

Toward A General Theory of Grain Alignment and Disruption by Radiative Torques and Magnetic Relaxation

THIEM HOANG,^{1,2}

¹Korea Astronomy and Space Science Institute, Daejeon 34055, Republic of Korea

²Department of Astronomy and Space Science, University of Science and Technology, 217 Gajeong-ro, Yuseong-gu, Daejeon, 34113, Republic of Korea

(Dated: Draft version May 7, 2025)

ABSTRACT

We generalize the magnetically enhanced radiative torque (MRAT) alignment theory for general astrophysical environments described by a dimensionless parameter $U/(n_1 T_2)$ with U local radiation strength, $n_1 = n_H/(10 \text{ cm}^{-3})$ the hydrogen density, and $T_2 = T_{\text{gas}}/100\text{K}$ the gas temperature. We first derive the critical magnetic relaxation $\delta_{\text{mag,cri}}$ required to produce high-J attractors for different RAT models and local conditions and find that $\delta_{\text{mag,cri}}$ must be larger for stronger radiation fields. We then numerically study the grain alignment and rotational disruption by the MRAT mechanism, taking into account gas collisions and magnetic fluctuations. We find that, for the collision-dominated (CD) regime ($U/(n_1 T_2) \leq 1$), collisional and magnetic excitations can slowly transport large grains from low-J rotation to high-J attractors, leading to the perfect *slow alignment* within $\sim 10 - 100$ damping times due to MRATs. However, for the radiation-dominated (RD) regime ($U/(n_1 T_2) > 1$), only a fraction of grains can be fast aligned at high-J attractors by MRATs, and the majority of grains are trapped at low-J rotation due to strong radiative torques, a new effect we term *radiative torque (RAT) trapping*. For extreme radiation fields of $U/(n_1 T_2) > 10^4$, the efficiency of magnetic relaxation on grain alignment is suppressed, and grains only have fast alignment and disruption purely determined by RATs. We quantified the fraction of grains with fast alignment at high-J attractors, $f_{\text{high-J}}^{\text{fast}}$, for different RAT models, magnetic relaxation, and $U/(n_1 T_2)$, and found that the maximum $f_{\text{high-J}}^{\text{fast}}$ can reach 45% by MRATs and 22% by RATs. We discuss the implications of our results for understanding alignment and rotational disruption of interstellar dust and stardust in different astrophysical environments.

1. INTRODUCTION

The alignment of non-spherical dust grains with ambient magnetic fields causes starlight polarization (Hall 1949; Hiltner 1949) and thermal dust emission polarization (Planck Collaboration et al. 2015). Dust polarization induced by grain alignment is widely used to trace the two-dimensional (2D) magnetic fields (B-fields) projected in the plane of the sky from the diffuse interstellar medium (ISM) and molecular clouds to star- and planet-forming regions (Pattle et al. 2023; Tsukamoto et al. 2023). The polarization degree offers valuable information on dust properties (size, shape, and composition), and the physical processes responsible for grain alignment (Hoang & Truong 2024). Recently, new techniques were introduced for probing three-dimensional (3D) B-

fields by combining 2D B-fields traced by the polarization angles with the inclination angle constrained by the polarization degree (Hoang & Truong 2024; Truong & Hoang 2024).

Grain alignment by radiative torques (RATs), first noticed by Dolginov & Mitrofanov (1976a), and then numerically demonstrated by Draine & Weingartner (1996), is the standard theory for grain alignment in the ISM (Draine & Weingartner 1997; Andersson et al. 2015; Lazarian et al. 2015). The development of an analytical model (AMO) of RATs by Lazarian & Hoang (2007) enabled the era of quantitative grain alignment (Hoang & Lazarian 2008a, 2009b,a). The unified theory of grain alignment, namely magnetically enhanced RAT alignment (MRAT), was developed by Lazarian & Hoang (2008); Hoang & Lazarian (2016a) by combining RATs and enhanced magnetic relaxation due to iron inclusions embedded within dust grains. For an ensemble of different grain shapes and magnetic prop-

erties, there exists only a fraction of grains that can be aligned at an attractor with angular momentum greater than the thermal value (so-called high-J attractors), denoted by $f_{\text{high-J}}^{\text{ens}}$ (Hoang & Lazarian 2016a). For the typical diffuse ISM, Hoang & Lazarian (2016a) found that, if $\delta_{\text{mag}} > 10$, high-J attractors become universal regardless of the RAT models (e.g., grain shapes and compositions), so $f_{\text{high-J}}^{\text{ens}} = 1$. However, for $\delta_{\text{mag}} < 1$, high-J attractors are only determined by RATs, and $f_{\text{high-J}}^{\text{ens}} \sim 0.2 - 0.6$ (Herranen et al. 2021).

For a given shape and magnetic property that exhibit high-J attractors, if grains have initially random orientation with the magnetic field, a fraction of grains can be rapidly aligned at high-J attractor (so-called *fast alignment*). The rest of the grains are driven toward an attractor at thermal angular momentum (aka. low-J attractor). Numerical simulations in (Hoang & Lazarian 2008a, 2016a) for the typical ISM with the gas density $n_{\text{H}} = 30 \text{ cm}^{-3}$, gas temperature $T_{\text{gas}} = 100 \text{ K}$, and interstellar radiation field (ISRF) identified the crucial role of *collisional excitations* by gaseous random collisions in scattering grains out of the low-J attractors and slowly transporting them to high-J attractors, which can lead to the perfect alignment of grains within several gaseous damping times, *slow alignment* (also Lazarian & Hoang 2021). However, for grains without high-J attractors, grain alignment is negligible due to the strong randomization by gas collisions (Hoang & Lazarian 2008a, 2016a). As a result, the net alignment degree of grains can be determined by $f_{\text{high-J}}^{\text{ens}}$. The MRAT theory is successfully applied to the ISM and dense star-forming regions (SFRs) (Giang & Hoang 2024), and incorporated in the publicly available POLARIS code to model dust polarization (Reissl et al. 2016; Giang et al. 2024).

A new important physical effect arising from suprathermal rotation of grains by RATs is rotational disruption induced by centrifugal force, aka. radiative torque disruption (RATD) (Hoang et al. 2019; Hoang 2019). As a result, radiative torques govern both dust grain alignment and dust evolution, which have broader implications for astrophysics because dust is involved in the most important physical and chemical processes, as well as acting as a momentum carrier for radiation pressure feedback (Draine 2011). The observational evidence for RATD mechanism was reported in different environments with strong radiation fields (see Tram & Hoang 2022 for a review), including the line of sight toward supernovae (Giang et al. 2020), the torus around active galactic nuclei (AGN; Giang & Hoang 2021), the envelope of evolved stars (Truong et al. 2022), photodissociation regions (Tram et al. 2021a,b; Ngoc et al. 2024). In particular, in the time-domain era, the efficiency of

RATD is essential for accurate modeling of the intrinsic luminosity of transients as well as understanding the dust evolution caused by transient feedback. For a given grain shape and composition, if grains initially have random orientation and one turn on the radiation flash, the fraction of grains with fast alignment at high-J attractors is described $f_{\text{high-J}}^{\text{fast}}$. Therefore, the RATD efficiency can be described by $f_{\text{disr}} = f_{\text{high-J}}^{\text{ens}} \times f_{\text{high-J}}^{\text{fast}}$. Lazarian & Hoang (2021) calculated $f_{\text{high-J}}^{\text{fast}}$ for the standard ISM, implying the increases of $f_{\text{high-J}}^{\text{fast}}$ with the magnetic relaxation δ_{mag} and can reach 50%. Nevertheless, the effects of magnetic relaxation on enhancing the value of $f_{\text{high-J}}^{\text{ens}}$ and $f_{\text{high-J}}^{\text{fast}}$ have not been quantified for strong radiation fields. Moreover, the efficiency of collisional excitations in transporting grains from low-J to high-J attractors has not been quantified for strong radiation fields.

The main goal of this paper is to develop a general theory of the MRAT alignment for various astrophysical environments, and quantify the efficiency of both *fast and slow* alignment and disruption driven by the MRAT mechanism using numerical simulations. The rest of the paper is structured as follows. In Section 2, we review the basic physical processes and characteristic timescales for grain alignment by radiative torques and magnetic relaxation. Section 3 describes the general MRAT theory, the lower and upper limits for the magnetic relaxation effect, and numerical methods to quantify grain alignment. In Section 4, we show the numerical results of grain alignment for the different models of RATs, magnetic properties, and radiation fields. An extended discussion is presented in Section 5, and a summary of our main results is presented in Section 6.

2. REVIEW OF GRAIN ALIGNMENT AND DISRUPTION PHYSICS

In this section, we first review the fundamental physical processes involved in grain alignment physics to be used in this paper for reference. For grains with iron inclusions considered in this paper, internal relaxation is fast due to Barnett relaxation (Dolginov & Mitrofanov 1976b) and inelastic relaxation (Lazarian & Efrimsky 1999) (see more details in Hoang et al. 2021b; Hoang et al. 2022), and we discuss only processes inducing external alignment of grain angular momentum (\mathbf{J}) with the magnetic field (\mathbf{B}), including magnetic relaxation and radiative torques.

2.1. Rotational Damping

Grain rotation is damped by gas collisions followed by evaporation. For an oblate spheroidal grain of mass density ρ , the characteristic timescale due to gas collisions

is given by

$$\tau_{\text{gas}} = \frac{3}{4\sqrt{\pi}} \frac{I_{\parallel}}{n_{\text{H}} m_{\text{H}} v_T a^4 \Gamma_{\parallel}},$$

$$\simeq 2.2 \times 10^5 \hat{\rho} \hat{s} a_{-5} \left(\frac{100 \text{ K}}{T_{\text{gas}}} \right)^{1/2} \left(\frac{10 \text{ cm}^{-3}}{n_{\text{H}}} \right) \left(\frac{1}{\Gamma_{\parallel}} \right) \text{ yr}, \quad (1)$$

where n_{H} is the hydrogen density, T_{gas} is the gas temperature, $v_T = (2k_B T_{\text{gas}}/m_{\text{H}})^{1/2}$ is the hydrogen thermal velocity, $a = a_{-5} 10^{-5} \text{ cm}$ is the length of the semi-major axis, and $s = b/a < 1$ is the ratio of the semi-minor to semi-major axes with $\hat{s} = s/0.5$, $I_{\parallel} = 8\pi\rho s a^5/15$ is the moment of inertia along the principal axis of maximum inertia moment (also denoted as I_1), and Γ_{\parallel} is a geometrical parameter of order unity (see [Roberge et al. 1993](#)).

Dust grains are heated by stellar radiation and cool down by infrared emission. Infrared emission reduces the grain's angular momentum. The grain rotational damping due to infrared emission is described by (see [Draine & Lazarian 1998](#)):

$$F_{\text{IR}} \simeq 1.2 U^{2/3} \left(\frac{10^{-5} \text{ cm}}{a_{\text{eff}}} \right) \left(\frac{10 \text{ cm}^{-3}}{n_{\text{H}}} \right) \left(\frac{100 \text{ K}}{T_{\text{gas}}} \right)^{1/2} \quad (2)$$

where $U = u_{\text{rad}}/u_{\text{MMP}}$ with u_{rad} the energy density of the radiation field is the radiation strength and $u_{\text{MMP}} = 8.64 \times 10^{-13} \text{ erg cm}^{-3}$ is the energy density of the standard ISRF in the solar neighborhood from [Mathis et al. \(1983\)](#), and a_{eff} is the effective size of an irregular grain defined as the radius of an equivalent sphere of the same volume $V_{\text{gr}} = 4\pi a_{\text{eff}}^3/3$. For numerical estimates of the characteristic timescales, we use the oblate spheroidal shape for convenience, so $a_{\text{eff}} = a s^{1/3}$, where $s = 1/2$ is fixed in this paper.

The total damping rate for grain rotation by gas collisions and infrared emission is given by

$$\tau_{\text{damp}}^{-1} = \tau_{\text{gas}}^{-1} (1 + F_{\text{IR}}). \quad (3)$$

The total damping torque by gas collisions and IR emission can be described by

$$\mathbf{\Gamma}_{\text{damp}} = -\frac{\mathbf{J}}{\tau_{\text{damp}}}. \quad (4)$$

2.2. Barnett magnetic moment and Larmor precession

2.2.1. Dust Grain Magnetism

Iron is among the most abundant elements in the universe. Spectroscopic observations show that more than 95% of iron is depleted from the gas ([Jenkins 2009](#)) and thus embedded into dust grains. Iron atoms, if distributed diffusely within a dust grain, produce ordinary

paramagnetic material (PM). The zero-frequency susceptibility $\chi(0)$ of such a paramagnetic dust is given by the Curie's law:

$$\chi_{\text{PM}}(0) = \frac{n_p \mu^2}{3k_B T_d}, \quad (5)$$

where the effective magnetic moment per iron atom μ reads

$$\mu^2 \equiv p^2 \mu_B^2 = g_e^2 \mu_B^2 [j(j+1)], \quad (6)$$

with j being the angular momentum quantum number of electrons in the outer partially filled shell, and $p \approx 5.5$ is taken for silicate (see [Draine 1996](#)).

Plugging the typical numerical values into Equation (5), we obtain

$$\chi_{\text{PM}}(0) \simeq 0.03 f_p \hat{n}_{23} \left(\frac{p}{5.5} \right)^2 \left(\frac{20 \text{ K}}{T_d} \right), \quad (7)$$

where $\hat{n}_{23} = n/10^{23} \text{ cm}^{-3}$ is the atomic density of material, f_p is the fraction of paramagnetic (Fe) atoms in the dust grain which is $f_p = 1/7$ for silicate of structure MgFeSiO_4 .

When grains are incorporated with iron clusters, they can become superparamagnetic material (SPM), and their magnetic susceptibility is significantly enhanced from PM grains. Let N_{cl} be the number of iron atoms per inclusion (cluster). The SPM magnetic susceptibility is given by

$$\chi_{\text{SPM}}(0) = \frac{n_{\text{cl}} m^2}{3k T_d}, \quad (8)$$

where n_{cl} is the volume density of iron clusters, and $m = N_{\text{cl}} \mu_0 = N_{\text{cl}} p \mu_B$ is the average magnetic moment per iron clusters and m_0 is the average magnetic moment of Fe.

Let ϕ_{sp} be the volume filling factor of iron inclusions of the same size. One obtains $n_{\text{cl}} = \mathcal{N}/V_{\text{gr}}$ with \mathcal{N} the total number of iron clusters given by

$$\mathcal{N} = \frac{\phi_{\text{sp}} V_{\text{gr}}}{N_{\text{cl}} V_{\text{Fe}}},$$

$$\simeq 3.5 \times 10^8 \phi_{\text{sp}} N_{\text{cl}}^{-1} a_{-5}^3. \quad (9)$$

where $V_{\text{Fe}} = 4\pi R_{\text{Fe}}^3/4$ with R_{Fe} is the radius of iron atom ([Hoang & Lazarian 2016a](#)).

By plugging m and $n_{\text{cl}} = \mathcal{N}/V$ into Equation (8), we obtain:

$$\chi_{\text{SPM}}(0) \approx 0.026 N_{\text{cl}} \phi_{\text{sp}} \hat{p}^2 \left(\frac{20 \text{ K}}{T_d} \right), \quad (10)$$

which is a factor N_{cl} greater than the PM susceptibility given by Equation 7.

2.2.2. Grain Magnetic Moment from Barnett effect and Larmor Precession

A rotating PM/SPM grain acquires a magnetic moment through the Barnett effect (Barnett 1915). The instantaneous Barnett magnetic moment of a grain of volume V_{gr} rotating with the angular velocity $\boldsymbol{\Omega}$ is equal to

$$\boldsymbol{\mu}_{\text{Bar}} = \frac{\chi(0)V_{\text{gr}}\boldsymbol{\Omega}}{\gamma_g} = -\frac{\chi(0)V_{\text{gr}}}{g_e\hbar\mu_B}\boldsymbol{\Omega}, \quad (11)$$

where $\chi(0)$ is given by Equation (7) for PM and (10) for SPM grains, $\gamma_g = -g_e\mu_B/\hbar \approx -e/(m_e c)$ is the gyromagnetic ratio of an electron, $g_e \approx 2$ is the g -factor, and $\mu_B = e\hbar/2m_e c \approx 9.26 \times 10^{-21} \text{ ergG}^{-1}$ is the Bohr magneton.

The interaction of the grain magnetic moment with an external static magnetic field \mathbf{B} results in a magnetic torque

$$\begin{aligned} \boldsymbol{\Gamma}_B &= [\boldsymbol{\mu}_{\text{Bar}} \times \mathbf{B}] \\ &= -|\boldsymbol{\mu}_{\text{Bar}}|B \sin \beta \hat{\phi} \equiv I_{\parallel} \omega \sin \beta d\phi/dt \hat{\phi} \end{aligned} \quad (12)$$

where $\hat{\phi}$ is the unit vector describing the increase of the precession angle β around \mathbf{J} (see Figure 1), resulting in the rapid Larmor precession of $\mathbf{J} \parallel \boldsymbol{\Omega}$ around \mathbf{B} .

The period of such a Larmor precession denoted by τ_{Lar} , is given by

$$\begin{aligned} \tau_{\text{Lar}} &= \frac{2\pi}{|d\phi/dt|} \\ &= \frac{2\pi I_{\parallel} g \mu_B}{\chi_0 V \hbar B} \simeq 0.65 a_{-5}^2 \hat{s}^{-2/3} \frac{\hat{\rho}}{\hat{\chi} \hat{B}} \text{ yr}, \end{aligned} \quad (13)$$

where $\hat{\chi} = \chi(0)/10^{-4}$, and $\hat{B} = B/10\mu\text{G}$ is the normalized magnetic field strength. Comparing Equation (13) with Equations (1) and (15), it is seen that the Larmor precession is much faster than the rotational damping and magnetic relaxation.

2.3. Magnetic Relaxation

Rotating magnetic (para-/superparamagnetic) grains experience the dissipation of the grain rotational energy into heat due to the lag, resulting in the alignment of \mathbf{J} with the ambient field. This is described by a magnetic torque (Davis & Greenstein 1951; Draine & Weingartner 1997):

$$\boldsymbol{\Gamma}_{\text{mag}} = -\frac{\mathbf{J}}{\tau_{\text{mag}}} \left(\sin \xi \cos \xi \hat{\xi} + \sin^2 \xi \hat{\mathbf{J}} \right), \quad (14)$$

where $\hat{\xi}$ is the unit vector describing the angle between \mathbf{J} and \mathbf{B} (see Figure 1), τ_{mag} is the characteristic time

of the magnetic relaxation given by

$$\begin{aligned} \tau_{\text{mag}} &= \frac{I_{\parallel}}{K(\omega)V_{\text{gr}}B^2} = \frac{2\rho a^2 s^{-2/3}}{5K(\omega)B^2}, \\ &\simeq 6 \times 10^5 \hat{\rho} \hat{s}^{-2/3} a_{-5}^2 \hat{B}^{-2} \hat{K}^{-1} \text{ yr}, \end{aligned} \quad (15)$$

where $V_{\text{gr}} = 4\pi s a^3/3$ is the grain volume, and $\hat{K} = K(\omega)/10^{-13} \text{ s}$ and $K(\omega) = \chi_2(\omega)/\omega$ with $\chi_2(\omega)$ as the imaginary part of the complex magnetic susceptibility of the grain material.

To describe the aligning effect of magnetic relaxation relative to the disalignment by gas collisions, the dimensionless magnetic relaxation strength was introduced in Hoang & Lazarian (2016a) as:

$$\begin{aligned} \delta_{\text{mag}} &= \frac{\tau_{\text{gas}}}{\tau_{\text{mag}}}, \\ &\simeq 0.3 \hat{\rho} a_{-5} \left(\frac{\hat{K} \hat{B}^2}{n_1 T_2^{1/2}} \right), \end{aligned} \quad (16)$$

where $n_1 = n_{\text{H}}/(10 \text{ cm}^{-3})$ and $T_2 = T_{\text{gas}}/100 \text{ K}$, where the physical parameters of the typical ISM are used. The exact value of δ_{mag} depends on the grain size, magnetic properties and magnetic field strength as well as the local gas conditions (see Hoang & Lazarian 2016a for more details).

2.4. Radiative Torques and the RAT Alignment

Anisotropic radiation propagating along \mathbf{k} exerts a radiative torque on an irregular grain. Let u_{λ} be the spectral energy density of the radiation field at wavelength λ and γ be its anisotropy. The energy density of the radiation field is $u_{\text{rad}} = \int u_{\lambda} d\lambda$. The radiative torque arising from the interaction of the anisotropic radiation field with an irregular grain of size a is then given by

$$\begin{aligned} \boldsymbol{\Gamma}_{\text{RAT}} &= \int \left(\frac{\gamma \pi a_{\text{eff}}^2 \lambda u_{\lambda}}{2\pi} \right) \mathbf{Q}_{\Gamma} d\lambda, \\ &= \left(\frac{\gamma a_{\text{eff}}^2 \bar{\lambda} u_{\text{rad}}}{2} \right) \bar{\mathbf{Q}}_{\Gamma} d\lambda \end{aligned} \quad (17)$$

where \mathbf{Q}_{Γ} is the RAT efficiency which can be decomposed into three components Q_{e1}, Q_{e2} and Q_{e3} in the alignment reference frame defined by unit vectors $\hat{\mathbf{e}}_1, \hat{\mathbf{e}}_2, \hat{\mathbf{e}}_3$ with $\hat{\mathbf{e}}_1 \parallel \mathbf{k}$, $\hat{\mathbf{e}}_2 \perp \hat{\mathbf{e}}_1$ and $\hat{\mathbf{e}}_3 = \hat{\mathbf{e}}_1 \times \hat{\mathbf{e}}_2$ (see Fig.1). Above, $\bar{\lambda}$ and $\bar{\mathbf{Q}}$ are the average wavelength and RAT efficiency over the local radiation spectrum, and $u_{\text{rad}} = U u_{\text{MMP}}$ is the radiation energy density of the local radiation field.

The magnitude of RAT efficiency, Q_{Γ} , in general, depends on the radiation field, grain shape, size and grain orientation relative to \mathbf{k} (Draine & Weingartner 1996; Lazarian & Hoang 2007). Due to the uncertainty in interstellar grain shapes, an analytical model

of RATs was introduced by Lazarian & Hoang (2007), and they demonstrated that their analytical torques exhibits the similar functional forms and basic features as calculated by Discrete Dipole Approximation code (DDSCAT) (Draine & Flatau 1994) for irregular shapes. Recently, the AMO is well supported with numerical calculations for an ensemble of shapes (Herranen et al. 2019). However, the relative amplitude of $Q_{e1}(\Theta)$ and $Q_{e2}(\Theta)$ changes from one shape to another and also varies with the wavelength. Therefore, we can the AMO and describe the RATs of different grain shapes and compositions through the ratio of the magnitudes of these torque components (Lazarian & Hoang 2007)

$$q^{\max} = \frac{Q_{e1}^{\max}}{Q_{e2}^{\max}}. \quad (18)$$

The magnitude of RAT efficiency for a given grain size and a wavelength can be approximately described by the empirical scaling law from (Lazarian & Hoang 2007), which is comparable to the recent results by Herranen et al. (2019) and Jager et al. (2024). Therefore, the combination of AMO and the RAT magnitude is sufficient to describe RATs for different grain shapes and sizes, and we assume that for dust grains (Hoang & Lazarian 2016a) and in this paper.

Following Lazarian & Hoang (2007), RATs can cause three different effects on grain dynamics, including the precession of the grain angular momentum around the radiation direction \mathbf{k} , spinup/spindown of the grain rotation, and the alignment of \mathbf{J} and \mathbf{k} . Rotating paramagnetic and superparamagnetic grains acquire a magnetic moment due to Barnett effect (Barnett 1915; Dolginov & Mitrofanov 1976b), resulting in the Larmor precession of the grain angular momentum around the ambient magnetic field \mathbf{B} . For PM/SPM grains, the Larmor precession is dominant over the radiative precession around \mathbf{k} , which establishes the \mathbf{B} as an axis of the grain alignment. If the radiative precession is faster than the Larmor precession, the alignment axis is \mathbf{k} . Figure 1 describes the orientation of the grain angular momentum with \mathbf{B} due to RATs from a radiation beam along \mathbf{k} .

It is convenient to study the grain orientation in the lab system using spherical coordinates, which is completely determined by three variables: the angle ξ between the angular momentum vector \mathbf{J} and the magnetic field direction \mathbf{B} , the Larmor precession angle ϕ of \mathbf{J} around \mathbf{B} and the value of the angular momentum J . To describe the effect of grain alignment by RATs in the lab coordinate system, one decomposes RATs into the net torque component along \mathbf{J} responsible for spinup/spindown, denoted by $H(\xi, \phi, \psi)$, the torque component perpendicular to \mathbf{J} directed along $\hat{\xi}$

responsible for alignment/disalignment of \mathbf{J} with \mathbf{B} , denoted by $F(\xi, \phi, \psi)$, and the torque component directed along $\hat{\phi}$ causing the radiative precession, $G(\xi, \phi, \psi)$. Therefore, Equation (17) can be rewritten as

$$\mathbf{\Gamma}_{\text{RAT}} = M \left[H(\xi, \phi, \psi) \hat{\mathbf{J}} + F(\xi, \phi, \psi) \hat{\xi} + G(\xi, \phi, \psi) \hat{\phi} \right] 9$$

where

$$M = \frac{\gamma \bar{\lambda} u_{\text{rad}} a_{\text{eff}}^2}{2}. \quad (20)$$

For more details, see previous papers (Draine & Weingartner 1997; Lazarian & Hoang 2007; Hoang & Lazarian 2008a, 2016a; Hoang 2022).

Figure 2 shows the averaged torque components, $\langle H \rangle$ and $\langle F \rangle$, for a RAT model with $q^{\max} = 3$, obtained from averaging H and F over fast Larmor precession and thermal fluctuations of the grain axis of maximum inertia with \mathbf{J} , as function of the angle $\cos \xi$ between \mathbf{J} and the magnetic field for the case $q^{\max} = 3$ and $\psi = 0^\circ$, assuming the different values of J (see Hoang & Lazarian 2008a, 2016a for details). For this RAT model, $\langle H \rangle > 0$ for $\cos \xi > 0$ and $\langle H \rangle < 0$ for $\cos \xi < 0$. There are four stationary points determined by $\langle F \rangle = 0$ (marked by circles), among which $\cos \xi = 1$ is an attractor with $\langle H \rangle > 0$. Under the sole effect of RATs, grain alignment typically occurs at low- J and high- J attractors; however, the existence of high- J attractors is not universal and depends on grain shapes and radiation fields (Lazarian & Hoang 2007).

2.5. Radiative Torque Disruption

An effectively spherical grain of radius a_{eff} spinning at angular velocity Ω experiences a centrifugal stress $S = \rho a_{\text{eff}}^2 \Omega^2 / 4$ acting on the plane through the grain center. Let S_{max} be the tensile strength of the grain material. The critical angular speed above which the grain is disrupted is determined by setting $S = S_{\text{max}}$, yielding,

$$\Omega_{\text{disr}} = \frac{2}{a_{\text{eff}}} \left(\frac{S_{\text{max}}}{\rho} \right)^{1/2} \simeq \frac{3.65 \times 10^8}{a_{\text{eff},-5}} \left(\frac{S_{\text{max},7}}{\hat{\rho}} \right)^{1/2} \text{ rads}^{-1}, \quad (21)$$

where $a_{\text{eff},-5} = a_{\text{eff}} / 10^{-5} \text{ cm}$, and $S_{\text{max},7} = S_{\text{max}} / (10^7 \text{ erg cm}^{-3})$.

RATs can rapidly spin up grains to suprathreshold rotation with angular velocity greater than Ω_{disr} , resulting in instantaneous destruction of the grain into small fragments (Hoang et al. 2019; Hoang 2019). Therefore, the disruption can occur whenever the grain's angular velocity exceeds the critical value.

For strong radiation fields of $F_{\text{IR}} > 1$, the characteristic timescale for fast disruption of grains is defined as

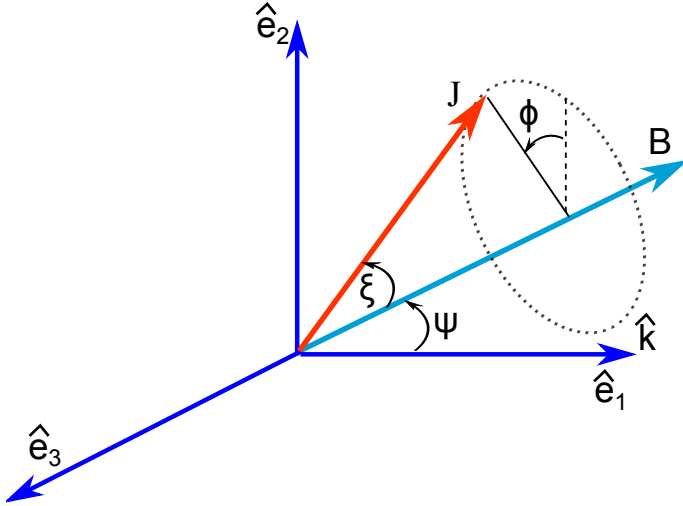


Figure 1. Orientation of the grain angular momentum \mathbf{J} in a lab coordinate system $\hat{\mathbf{e}}_1\hat{\mathbf{e}}_2\hat{\mathbf{e}}_3$. The axis $\hat{\mathbf{e}}_1$ is defined by the radiation direction \mathbf{k} , the axis $\hat{\mathbf{e}}_2$ is perpendicular to $\hat{\mathbf{e}}_1$ and lies in the plane $\hat{\mathbf{e}}_1$ and magnetic field \mathbf{B} . The radiation direction makes an angle ψ with the magnetic field. The alignment angle is described by ξ , and fast Larmor precession of \mathbf{J} around \mathbf{B} is described by the angle ϕ .

(Hoang et al. 2019; Hoang 2019)

$$t_{\text{disr}}^{\text{fast}} = \frac{I_{\parallel}\Omega_{\text{disr}}}{\Gamma_{\text{RAT}}} = \left(\frac{\Omega_{\text{disr}}}{\Omega_{\text{RAT}}} \right) \tau_{\text{damp}}, \quad (22)$$

$$\simeq 10^5 (\gamma U)^{-1} \bar{\lambda}_{0.5}^{-1.7} \hat{\rho}^{1/2} S_{\text{max},7}^{1/2} a_{\text{eff},-5}^{-0.7} \text{yr}$$

for $a_{\text{disr}} < a_{\text{eff}} \lesssim a_{\text{trans}}$, and

$$t_{\text{disr}}^{\text{fast}} \simeq 7.4 (\gamma U)^{-1} \bar{\lambda}_{0.5}^{-1.7} \hat{\rho}^{1/2} S_{\text{max},7}^{1/2} a_{\text{eff},-5}^2 \text{yr} \quad (23)$$

for $a_{\text{trans}} < a_{\text{eff}} < a_{\text{disr,max}}$ (Hoang et al. 2019).

3. GENERAL THEORY OF THE MRAT ALIGNMENT

3.1. Basic Equations of Grain Rotational Dynamics

As discussed in Section 2, the external alignment of grains with the magnetic field is mainly governed by rotational damping processes, magnetic relaxation, and RATs. Numerical calculations of grain alignment by MRATs are studied by following the evolution of grain angular momentum in the phase space (Draine & Weingartner 1997; Lazarian & Hoang 2007; Hoang et al. 2016).

The evolution of the grain angular momentum in the lab coordinate system defined by the magnetic field and radiation direction (see Figure 1) is described by the equation of motion (Draine & Weingartner 1997; Lazarian & Hoang 2007)

$$\frac{d\mathbf{J}}{dt} = \mathbf{\Gamma}_{\text{RAT}} + \mathbf{\Gamma}_B + \mathbf{\Gamma}_{\text{damp}} + \mathbf{\Gamma}_{\text{mag}}, \quad (24)$$

where the RAT torque is given by Equation 17), $\mathbf{\Gamma}_{\text{damp}}$ by Equation 4, and $\mathbf{\Gamma}_{\text{mag}}$ by Equation (14).

In the spherical coordinate system with unit basis vectors $(\hat{\mathbf{J}} = \mathbf{J}/|\mathbf{J}|, \hat{\xi}, \hat{\phi})$, \mathbf{J} is described by three variables J, ξ, ϕ (see Figure 1, and the time-evolution of bJ is represented as (Weingartner & Draine 2003; Hoang & Lazarian 2008b)

$$\frac{d\mathbf{J}}{dt} = \frac{dJ}{dt} \hat{\mathbf{J}} + \frac{J}{dt} \frac{d\xi}{dt} \hat{\xi} + J \sin \xi \frac{d\phi}{dt} \hat{\phi}. \quad (25)$$

After averaging Equations (24) and (25) over the angle ϕ due to the fast Larmor precession, it reduces to two equations that determine the alignment of \mathbf{J} with the magnetic field:

$$\frac{d\xi}{dt} = \frac{M \langle F \rangle(\xi, \psi)}{J} - \frac{\sin \xi \cos \xi}{\tau_{\text{mag}}}, \quad (26)$$

$$\frac{dJ}{dt} = M \langle H \rangle(\xi, \psi) - \frac{J}{\tau_{\text{damp}}} - \frac{J}{\tau_{\text{mag}}} \sin^2 \xi, \quad (27)$$

where

$$M = \frac{\gamma \bar{\lambda} u_{\text{rad}} a_{\text{eff}}^2}{2}, \quad (28)$$

where $\langle F \rangle(\xi, \psi)$ and $\bar{H}(\xi, \psi)$ are aligning and spin-up torque components averaged over the precession angle ψ , and τ_{damp} is the rotational damping time of grains due to both gas collisions and IR emission. These equations are different from previous studies (Hoang & Lazarian 2016a; Lazarian & Hoang 2021) in which only gas damping is taken into account.

As in previous studies (Hoang & Lazarian 2008a, 2016a), we use the dimensionless parameter, $J' = J/J_T$ with $J_T = I_{\parallel} \omega_T$ and $\omega_T = (kT_{\text{gas}}/I_{\parallel})^{1/2} \simeq 10^5 s^{-1/2} a_{-5}^{-5/2} T_2^{1/2}$ as thermal angular momentum along one axis. The dimensionless time is defined by $t' = t/\tau_{\text{damp}}$, which is different from previous work in which τ_{gas} is used due to the subdominance of IR emission in the standard ISM. Equations (26) and (27) become

$$\frac{d\xi}{dt'} = \left(\frac{M \tau_{\text{damp}}}{J_T} \right) \frac{\langle F \rangle(\xi, \psi)}{J'} - \frac{\tau_{\text{damp}}}{\tau_{\text{mag}}} \sin \xi \cos \xi, \quad (29)$$

$$\frac{dJ'}{dt'} = \left(\frac{M \tau_{\text{damp}}}{J_T} \right) \langle H \rangle(\xi, \psi) - J' \left(1 + \frac{\tau_{\text{damp}}}{\tau_{\text{mag}}} \sin^2 \xi \right). \quad (30)$$

Denote the prefactor in the first terms of the above equation by

$$\delta_{\text{RAT}} \equiv \frac{M \tau_{\text{damp}}}{J_T} \simeq 6.2 \times 10^4 a_{-5}^{1/2} \frac{U}{n_1 T_2}, \quad (31)$$

which characterizes the relative importance of RATs and the damping by gas collisions and IR emission. Therefore, the term $U/(n_1 T_2)$ can be used to characterize the

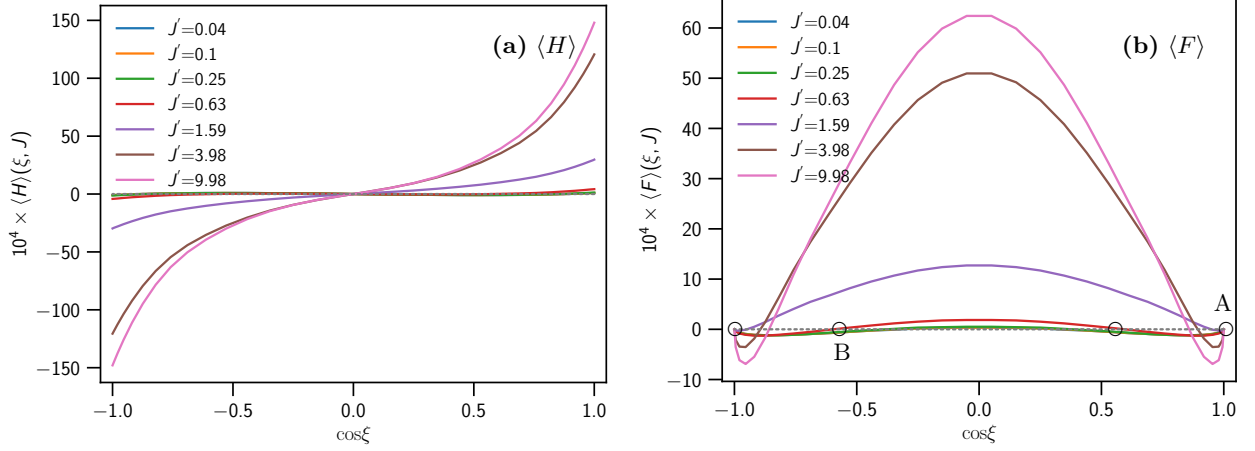


Figure 2. The averaged aligning (panel (a)) and spinup (panel (b)) torque components for the different grain angular momentum, assuming the RAT model of $q^{\max} = 3$ and the radiation parallel to the magnetic field, $\psi = 0^\circ$. The intersection between the dotted line and $\langle F \rangle$ determines the stationary points marked by circles for the case $J' = 0.63$.

difference of the local environment from the standard ISM with $n_{\text{H}} = 10 \text{ cm}^{-3}$ and $T_{\text{gas}} = 100 \text{ K}$.

Using the standard definition of the magnetic relaxation strength from Equation (16), one then writes

$$\frac{\tau_{\text{damp}}}{\tau_{\text{mag}}} = \frac{\delta_{\text{mag}}}{1 + F_{\text{IR}}}, \quad (32)$$

which implies the reduction of magnetic relaxation by a factor $1 + F_{\text{IR}}$.

In the steady state, the maximum angular momentum spun-up by RATs can be obtained by setting $d\xi/dt' = 0$, $dJ'/dt' = 0$, which yields

$$J'_{\text{RAT}}^{\max} = \delta_{\text{RAT}} \langle H \rangle. \quad (33)$$

The above equations of motion can be rewritten as

$$\frac{d\xi}{dt'} = \frac{\delta_{\text{RAT}} \langle F \rangle(\xi, \psi)}{J'} - \frac{\delta_{\text{mag}}}{1 + F_{\text{IR}}} \sin \xi \cos \xi, \quad (34)$$

$$\frac{dJ'}{dt'} = \delta_{\text{RAT}} \langle H \rangle(\xi, \psi) - J' \left(1 + \frac{\delta_{\text{mag}}}{1 + F_{\text{IR}}} \sin^2 \xi \right) \quad (35)$$

which reveal that grain alignment fully determined by three parameters, δ_{RAT} , δ_{mag} , and RAT efficiency $\langle F \rangle$, \bar{H} . Therefore, Equations (34) and (35) can be used to simulate the alignment process of grains subject to a wide range of environments by varying the parameters δ_{RAT} .

3.2. Critical Magnetic Relaxation for Producing High-J Attractors in the MRAT Mechanism

3.2.1. Critical Magnetic Relaxation for the MRAT

Previous studies (Hoang & Lazarian 2016a; Herranen et al. 2021) derive the critical relaxation required for producing high-J attractors by MRATs for the ISM for

which the IR damping is subdominant. Here, we derive the criteria for high-J attractors when taking into account the effect of IR damping.

Following the method in Hoang & Lazarian (2016a), we determine the criteria for the stationary point at $\sin \xi_s = 0$, $J'_s = \delta_{\text{RAT}} \bar{H}(\xi_s)$ for which $(d\xi/dt' = 0, dJ'/dt' = 0)$ (see Eqs.35) to be an attractor as follows:

$$\left. \frac{1}{\langle H \rangle} \frac{d\langle F \rangle}{d\xi} \right|_{\sin \xi_s = 0} - \frac{\delta_{\text{mag}}}{1 + F_{\text{IR}}} < 0, \quad \langle H \rangle > 0, \quad (36)$$

which simply indicates that to produce an attractor point, the rate of increasing ξ from ξ_s by RATs must be lower than the rate of decreasing ξ by magnetic relaxation δ_{mag} .

When the radiation direction is along the magnetic field ($\psi = 0$), the above conditions yield the critical strength required for high-J attractor (Hoang & Lazarian 2016a):

$$\frac{\delta_{\text{mag,cri}}}{1 + F_{\text{IR}}} = \frac{2 - q^{\max}}{q^{\max}}, \quad (37)$$

which yields

$$\delta_{\text{mag,cri}} = \frac{2 - q^{\max}}{q^{\max}} (1 + F_{\text{IR}}). \quad (38)$$

$$(39)$$

One note that the above condition is always satisfied if $q^{\max} > 2$. However, for $q^{\max} < 2$, RATs do not produce high-J attractors, and the magnetic relaxation is crucial. Therefore, the critical magnetic relaxation has an additional term $1 + F_{\text{IR}}$ different from Hoang & Lazarian (2016a). In typical and weak radiation fields, $F_{\text{IR}} \ll 1$ and it is not important, but in a strong radiation field,

$F_{\text{IR}} \gg 1$, which influences the efficiency of magnetic relaxation in grain alignment. Since δ_{mag} has an upper limit determined by embedded iron inclusions, the magnetic relaxation effect will become ineffective in a strong radiation field.

Equation (38) provides the critical magnetic relaxation required for producing high-J attractors by the MRAT when the radiation is parallel to the magnetic field. For a general angle ψ , we numerically solve Equation (36) to $\delta_{\text{mag,cri}}$, as in Hoang & Lazarian (2016a). Figure 3 shows the results for the standard ISRF (upper left) and intense radiation fields with $U = 10^2, 10^3, 10^4$, assuming the gas density $n_{\text{H}} = 10 \text{ cm}^{-3}$ and $T_{\text{gas}} = 100 \text{ K}$. The critical magnetic relaxation must increase with increasing radiation strength in order to create high-J attractors, except in the parameter space where RATs alone can produce high-J attractors (white areas in the upper left and lower right). As a result, for a given δ_{mag} determined by the grain magnetic properties, the efficiency of magnetic relaxation on grain alignment is weaker for stronger radiation fields.

3.2.2. Upper Threshold of the MRAT

We can determine the threshold of the radiation strength for which magnetic relaxation is still effective, so that grain alignment is described by MRATs as follows. For a strong radiation field of $U/(n_1 T_2) > 1$, $F_{\text{IR}} \sim U^{2/3}/n_1 \gg 1$, and Equation (38) can be rewritten as

$$\delta_{\text{mag,cri}} = \frac{2 - q^{\text{max}}}{q^{\text{max}}} F_{\text{IR}} \quad (40)$$

$$= \frac{2 - q^{\text{max}}}{q^{\text{max}}} \left(\frac{1.2 U^{2/3}}{a_{\text{eff},-5}} \right) \left(\frac{1}{n_1 T_2^{1/2}} \right). \quad (41)$$

which depends on local radiation and gas density as $U^{2/3}/n_1$.

For grains with iron inclusions, following Hoang & Lazarian (2016a), one has

$$\delta_{\text{mag,SPM}} = 0.3 \hat{\rho} a_{\text{eff},-5} \left(\frac{10^5 N_{\text{cl},5} \hat{B}^2}{n_1 T_2^{1/2}} \right), \quad (42)$$

where $N_{\text{cl}} = 10^5 N_{\text{cl},5}$ is the number of iron atoms per cluster, and the 10^5 is the upper limit of iron clusters for SPM grains (Jones & Spitzer 1967; Yang 2021).

Setting $\delta_{\text{mag,SPM}} = \delta_{\text{mag,cri}}$, one obtains the upper limit for the radiation strength below which magnetic relaxation is still effective:

$$U_{\text{max}}^{\text{MRAT}} \simeq 5.2 \times 10^6 a_{\text{eff},-5}^3 N_{\text{cl},5}^{3/2} \hat{B}^3 \left(\frac{q^{\text{max}}}{2 - q^{\text{max}}} \right)^{3/2} \quad (43)$$

which corresponds to the dust temperature

$$T_{\text{max}}^{\text{MRAT}} \simeq 217.2 a_{\text{eff},-5}^{1/2} N_{\text{cl},5}^{1/4} \hat{B}^{1/2} \left(\frac{q^{\text{max}}}{2 - q^{\text{max}}} \right)^{1/4}. \quad (44)$$

Therefore, MRAT alignment is only effective for the radiation fields with $U < U_{\text{max}}^{\text{MRAT}}$. Above this limit, grain alignment is only determined by RATs.

3.3. Effects of Collisional and Magnetic Excitations on the MRAT Alignment

The effect of gas collisions in the framework of paramagnetic alignment was studied by many authors (Cugnon 1983; Lazarian 1997) using the Fokker-Planck equations. The Langevin equation (LE) approach was used to study this problem numerically in Roberge et al. (1993) and Roberge & Lazarian (1999). It was later applied to study the effect of collisional excitations in the framework of RAT alignment (Hoang & Lazarian 2008a), spinning dust emission (Hoang et al. 2011; Hoang et al. 2014), and magnetic dust emission (Hoang & Lazarian 2016b). Here, we follow a similar approach in Hoang & Lazarian (2016a).

Let $(\hat{x}, \hat{y}, \hat{z})$ be the inertial frame of reference where \hat{z} is defined parallel to the magnetic field. An increment of grain angular momentum after time interval dt due to various random interactions can be described by the LE (Roberge et al. 1993)

$$dJ_i = A_i(t)dt + B_{ij}(J, t)d\omega_j, \quad i = x, y, z, \quad (45)$$

where $d\omega_j$ are Wiener coefficients, and A_i, B_{ij} are the diffusion coefficients defined as

$$A_i = \langle \Delta J_i \rangle, \quad i = x, y, z, \quad (46)$$

$$(BB^T)_{ij} = \langle \Delta J_i \Delta J_j \rangle, \quad i, j = x, y, z, \quad (47)$$

where B^T is the transposal matrix of B (see Appendix B in Hoang & Lazarian 2016a).

The collisional excitation coefficients in the dimensionless units of $J' \equiv J/I_{\parallel} \omega_T$ and $t' \equiv t/\tau_{\text{damp}}$ due to gas collisions are then given by

$$\begin{aligned} B'_{\text{coll},i} &= B_{\text{coll},i} \times \left(\frac{\tau_{\text{damp}}}{2I_{\parallel} k T_{\text{gas}}} \right), \\ &= B_{\text{coll},i} \times \left(\frac{\tau_{\text{gas}}}{2I_{\parallel} k T_{\text{gas}}} \right) \frac{1}{1 + F_{\text{IR}}} \text{ for } i = x, y, \end{aligned} \quad (48)$$

where $B_{\text{coll},i}$ are given by Equations in Appendix B of Hoang & Lazarian (2016a), but the difference is τ_{gas} is replaced by τ_{damp} .

The coefficients for magnetic excitations are described by (see Appendix B in Hoang & Lazarian 2016a)

$$\begin{aligned} B'_{\text{mag,xx}} &= B'_{\text{mag,yy}} = \left(\frac{\delta_{\text{mag}}}{1 + F_{\text{IR}}} \right) \left(\frac{T_d}{T_{\text{gas}}} \right), \\ B'_{\text{mag,zz}} &= 0, \end{aligned} \quad (49)$$

for which we denote $\tilde{\delta}_{\text{mag}} = \delta_{\text{mag}}/(1 + F_{\text{IR}})$.

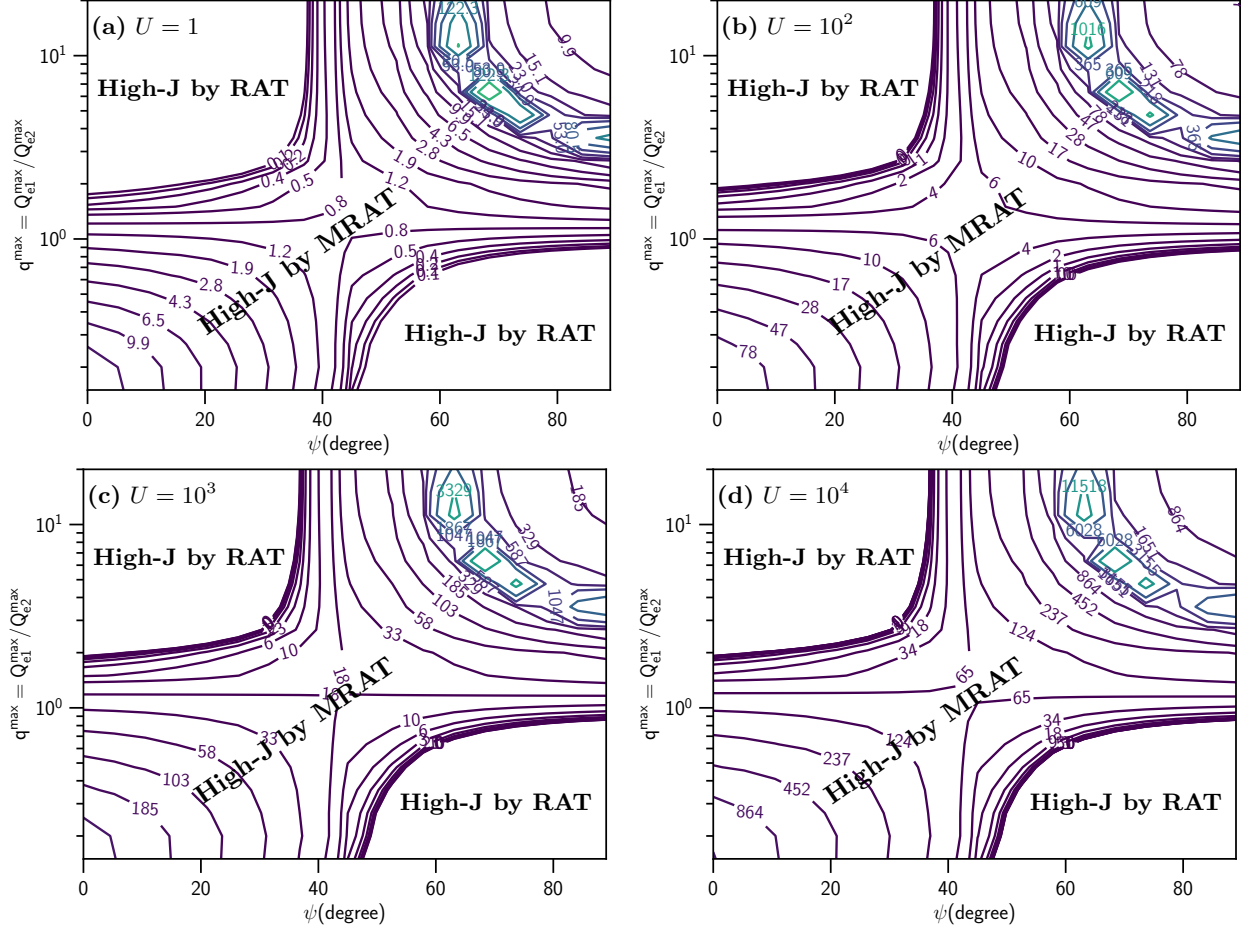


Figure 3. The map of the critical magnetic relaxation required to produce high-J attractors for the different RAT models (q^{\max}) and the angle between radiation direction with the magnetic field ψ in the different radiation fields of $U = 1 - 10^4$ (panels (a)-(d)). The white areas denote high-J attractors can be produced by RATs without needing magnetic relaxation. The contours are given for borders of the area corresponding to different δ_{mag} . The critical magnetic relaxation strength must be increased to have universal high-J attractors in stronger radiation fields.

The total excitation coefficients become $B'_{ii} = B'_{ii,\text{coll}} + B'_{ii,\text{mag}}$ where B_{ii} with $i = x, y, z$ denotes the diagonal matrix components. The magnetic fluctuations increase with δ_{mag} , but both collisional and magnetic excitations are reduced significantly in strong radiation fields with $F_{\text{IR}} > 1$.

In dimensionless units, Equation (45) becomes

$$dJ'_i = A'_i dt' + \sqrt{B'_{ii}} dw'_i \text{ for } i = x, y, z, \quad (50)$$

where $\langle dw_i'^2 \rangle = dt'$ and

$$\begin{aligned} A'_i &= -J'_i \left[1 + \tilde{\delta}_{\text{mag}}(1 - \delta_{iz}) \right], \\ B'_{ii} &= B'_{\text{coll},i} + \tilde{\delta}_{\text{mag}}(1 - \delta_{iz}) \left(\frac{T_d}{T_{\text{gas}}} \right), \end{aligned} \quad (51)$$

with $\delta_{iz} = 1$ for $i = z$ and $\delta_{iz} = 0$ for $i = x, y$.

3.4. Numerical Simulations of Grain Alignment and Disruption

As in Hoang & Lazarian (2008a, 2016a), to account for the randomization effect by gas collisions and magnetic fluctuations on grain alignment, we employ the hybrid approach. For each time step, we first solve the LEs subject to gas-grain collisions and magnetic fluctuations by solving for three components J_x, J_y, J_z using the 4th order Runge-Kutta integrator implemented in Hoang & Lazarian (2016a) and compute the current values of $\tilde{J} = \sqrt{J_x^2 + J_y^2 + J_z^2}$, $\cos \tilde{\xi} = J_z / \tilde{J}$. Then, we use \tilde{J} and $\tilde{\xi}$ as input parameters to solve Equations (26) and (27) for new values of ξ, J as a result of regular RATs only, where the terms involving the gas and magnetic damping are removed because those effects are already accounted for by the LEs. For estimates of rotational damping and excitation coefficients by gas collisions and magnetic fluctuations, we consider the oblate spheroidal shape for grains as in Hoang & Lazarian (2016a).

To check whether grains converge to some attractor point, we introduce the convergence criteria as follows:

$$\frac{|J'_{i+1} - J'_i|}{J'_i} \leq \epsilon_J, \quad \frac{|\cos(\xi_{i+1}) - \cos(\xi_i)|}{|\cos(\xi_i)|} \leq \epsilon_\xi, \quad (52)$$

where i is the timestep, and we adopt $\epsilon_J = 10^{-6}$ and $\epsilon_\xi = 10^{-6}$.

3.4.1. Calculations of Grain Alignment Degrees

The alignment of grain axes with the magnetic field includes internal alignment and external alignment. Let $Q_J = (3\cos^2\xi - 1)/2$ be the measure of the alignment of \mathbf{J} with the magnetic field, and $Q_X = (3\cos^2\theta - 1)/2$ be the alignment of the grain axis of maximum inertia with the angular momentum.

At each time step, we calculate Q_J by averaging over the ensemble of N_{gr} grains:

$$Q_J = \frac{1}{N_{\text{gr}}} \sum_{i=1}^{N_{\text{gr}}} \frac{(3\cos^2\xi_i - 1)}{2}. \quad (53)$$

The Rayleigh reduction factor (Greenberg 1968), which describes the alignment of the grain principal axis with the magnetic field (Roberge & Lazarian 1999), is calculated as

$$R = \frac{1}{N_{\text{gr}}} \sum_{i=1}^{N_{\text{gr}}} Q_J(\xi_i) Q_X(J_i), \quad (54)$$

and Q_X characterizes the alignment of grain axes with respect to \mathbf{J} . For an oblate grain with fast internal relaxation,

$$Q_X(J_i) = \int_0^\pi q_X Z \exp(-J_i^2[1 + (h-1)\sin^2\theta]) \sin\theta d\theta, \quad (55)$$

where $h = I_{\parallel}/I_{\perp}$ with $I_{\parallel,\perp}$ the principal inertia moments parallel and perpendicular to the grain symmetry axis, and the distribution of the angle θ between the grain axis of major inertia with \mathbf{J} is described by the local thermal equilibrium function, which is valid for grains with fast internal relaxation due to Barnett relaxation and inelastic relaxation (see Hoang & Lazarian 2016a).

3.4.2. Model Parameters and Setup

In dimensionless units, J', t' , the alignment of grains is not determined by three parameters, $\delta_{\text{RAT}}, \delta_{\text{mag}}$, and RAT efficiency $\langle F \rangle, \langle H \rangle$. Therefore, Equations 35 can be used to simulate the alignment process of grains subject to a wide range of environments by varying the parameters δ_{RAT} . To identify the effects of local physical conditions, we fix the effective grain size of $a_{\text{eff}} = 0.2 \mu\text{m}$

and the angle between the radiation direction and magnetic field at $\psi = 0^\circ$. We consider different RAT models of $q^{\text{max}} = 1, 2, 3$, corresponding to the case of RAT alignment without high-J attractor ($f_{\text{high-J}}^{\text{ens}} = 0$), with a small $f_{\text{high-J}}^{\text{ens}} = 0.1$, and $f_{\text{high-J}}^{\text{ens}} = 0.1$, respectively (Lazarian & Hoang 2021). Two typical models of magnetic relaxation of $\delta_{\text{mag}} = 1, 10^3$ correspond to PM and SPM grains containing a high level of iron inclusions. To account for a wide range of astrophysical environments, we consider a range of the ratio from $U/(n_1 T_2)$, including $U/(n_1 T_2) \lesssim 1$ which corresponds to the collision-dominated regions and $U/(n_1 T_2) > 1$ for radiation-dominated regions. Note that Hoang & Lazarian (2016a); Lazarian & Hoang (2021) run simulations for the typical ISM with $n_{\text{H}} = 30 \text{ cm}^{-3}$ and $U = 1$, corresponding to $U/(n_1 T_2) \approx 0.33$.

In addition to the gas density, gas and dust temperatures are also important parameters for estimating the characteristic timescales. In the ISM and radiation regions, gas is hotter than the gas due to photoelectric heating, but in dense and cold environments, gas and dust are thermally coupled. For a given radiation field, the dust temperature can be calculated assuming thermal equilibrium, which is a good approximation for the dust grains that can be aligned. Very small grains have a non-equilibrium temperature due to stochastic heating but are not aligned. The grain temperature of silicate and carbonaceous materials is given by (Draine 2011)

$$T_{\text{sil}} \simeq 16.4 U^{1/6} a_{\text{eff},-5}^{-1/15} \text{ K}, \quad (56)$$

$$T_{\text{carb}} \simeq 22.3 U^{1/6} a_{\text{eff},-5}^{-1/40} \text{ K}, \quad (57)$$

and the temperature for the mixed dust grain made of silicate and carbonaceous material is

$$T_d = (0.625 T_{\text{sil}}^4 + 0.375 T_{\text{carb}}^4)^{1/4}, \quad (58)$$

where we assume the volume fraction of silicate and carbonaceous material to be 62.5% and 37.5%, respectively. The gas temperature can be determined by T_d when the ratio T_{gas}/T_d is known. For the study here, we assume the gas temperature is higher than the dust as in the standard ISM with $T_{\text{gas}}/T_d \sim 5$.

We focus on a population of grains initially rotating at $J' = 3$ but having different orientations with the magnetic field (cf. Hoang & Lazarian 2008a, 2016a). We consider an ensemble of $N_{\text{gr}} = 16$ grains to better visualize the phase-map of their time-dependent alignment, especially in the presence of stochastic excitations. The total integration time is chosen to be long enough for the perfect grain alignment induced by collisional and magnetic excitations.

4. NUMERICAL RESULTS

We first run simulations of grain alignment for a fixed gas density $n_H = 10 \text{ cm}^{-3}$ with different ratios of $U/(n_1 T_2)$. We also tried to run simulations for different gas densities, such as $n_H = 10^2 - 1^4 \text{ cm}^{-3}$ and found that the alignment results are similar to those of $n_H = 10 \text{ cm}^{-3}$ given the same ratio $U/(n_1 T_2)$. Therefore, here, we show the numerical results for the typical density $n_H = 10 \text{ cm}^{-3}$ for the different ratio of $U/(n_1 T_2)$. We first show the typical RAT model of $q^{\text{max}} = 2$ for which RATs can induce high-J attractor (see Figure 3).

4.1. Collision-dominated (CD) Regime: $U/(n_1 T_2) \leq 1$

Here, we first show the results for the CD regime with $U/(n_1 T_2) \leq 1$. These CD regions include the standard ISM and star-forming regions, including MCs and filaments, to dense cores and protostellar environments.

Figure 4 shows the alignment maps for the CD regime described by $U/(n_1 T_2) = 0.16, 0.6, 1$. In all cases, random excitations by gas collisions (B_{coll}) and magnetic fluctuations (B_{mag}) occasionally drive grains from low-J into high-J attractors, and all grains eventually reach the perfect alignment at high-J attractors. This effect was previously reported in Hoang & Lazarian (2008a, 2016a) for the standard diffuse ISM with $n_H = 30 \text{ cm}^{-3}$, $U = 1$ or $U/(n_1 T_2) = 0.33$.

Figure 5 shows the time-dependent alignment degrees calculated from numerical simulations. For the first two cases (panels (a) and (b)), the alignment degrees increase rapidly with time and achieves perfect alignment (PA) after $T_{\text{PA}} \sim 10\tau_{\text{damp}} \sim 10\tau_{\text{gas}}$, but the later case of $U/(n_1 T_2) = 1$, it requires a time of $\sim 80\tau_{\text{damp}}$ to achieve significant alignment of $R = 0.8$.

Table 1 summarizes the model parameters adopted for our numerical calculations, the damping time, and the timescales required for perfect alignment for $q^{\text{max}} = 2$ for the SPM ($\delta_{\text{mag}} = 10^3$) and PM ($\delta_{\text{mag}} = 1$) grains. For the numerical values shown in this Table, $\tau_{\text{damp}} = \tau_{\text{gas}}(1 + F_{\text{IR}})$ for $U \leq 1$ and $\tau_{\text{damp}} \sim \tau_{\text{gas}}/F_{\text{IR}}$ for $U > 1$. The damping time is shorter for stronger radiation fields due to the increase of the infrared damping F_{IR} . For the CD regime of $U/(n_1 T_2) < 1$, the perfect alignment is achieved by slow transport after only $T_{\text{PA}} \sim 10\tau_{\text{damp}} \sim 10\tau_{\text{gas}}$ for SPM grains, but it requires $T_{\text{PA}} \sim 50\tau_{\text{gas}}$ for PM grains (see also Figures 18 and 11). For the RD regime of $U/(n_1 T_2) > 1$, grains are trapped at low-J rotations by strong radiative torques, and the perfect slow alignment is not achieved.

4.2. Radiation-Dominated (RD) Regime:

$$U/(n_1 T_2) > 1$$

Here we show the numerical results for the radiation-dominated regime of $U/(n_1 T_2) > 1$. Figure 6 shows the alignment map for $U/(n_1 T_2) = 1.9, 4.1, 7.3$ (panels (a)-(c)). As shown, a fraction of grains is rapidly driven to high-J attractors. The majority of grains is driven to low-J rotation during which collisional and magnetic excitations significantly disturb grain orientation. However, these excitation processes cannot transport grains to high-J attractors, and grains are radiatively trapped at the low-J rotation state. This is different from the CD regime observed in Figure 4. The trapping of grains at low-J rotation in this RD regime is the new effect, which we term radiative torque trapping (hereafter RATT).

The physics of RATT effect can be understood using the alignment function of RATs shown in Figure 2 (panel (b)). There are two stationary points at $\cos \xi = \pm 1$ and $\cos \xi \sim \pm 0.6$ for $J' = 0.63$. The stationary point $\cos \xi = 1, J' \gg 1$ is a high-J attractor point (circle A), and $\cos \xi = -0.6, J' < 1$ is a low-J attractor (circle B) produced by RATs (see Figure 2, panel (b)). When radiation field is strong, the low-J attractor is stabilized by RATs against gas random collisions, and grains are trapped at low-J attractors. However, for an average or weak radiation field, random collisions and magnetic fluctuations are dominant over RATs and can scatter grains out of this low-J attractor, slowly transporting them to the high-J attractor.

Figure 7 shows the time-dependent alignment degree calculated from the maps 6. The alignment degree increases rapidly within $0.01 - 0.02\tau_{\text{damp}}$ due to the fast alignment of grains to high-J attractors, and then it gets saturated due to the RAT trapping.

4.3. Effects of Magnetic Relaxation and Excitations

To study the effect of magnetic relaxation and excitations on the RAT alignment, we now show the results for the PM grains with $\delta_{\text{mag}} = 1$ to compare with the results for SPM grains in the previous section. We consider two different RAT models of $q^{\text{max}} = 2$ and $q^{\text{max}} = 1$ which have high-J attractor (former) and no high-J attractor (latter) as shown in Figure 3.

Figure 8 shows the alignment map for the RAT model with a high-J attractor described by $q^{\text{max}} = 2$ and $\delta_{\text{mag}} = 1$ in the CD regime. Collisional and magnetic excitations are sufficient to significantly scatter grain orientations to transport them to high-J attractors compared to the CD regime.

Figure 9 shows the time-dependent alignment degrees for $q^{\text{max}} = 2$ and $\delta_{\text{mag}} = 1$. Compared to Figure 5, one can see that the timescale for reaching the terminal alignment is longer by a factor of 5 for the PM grains. This can be understood due to the effect of strong super-

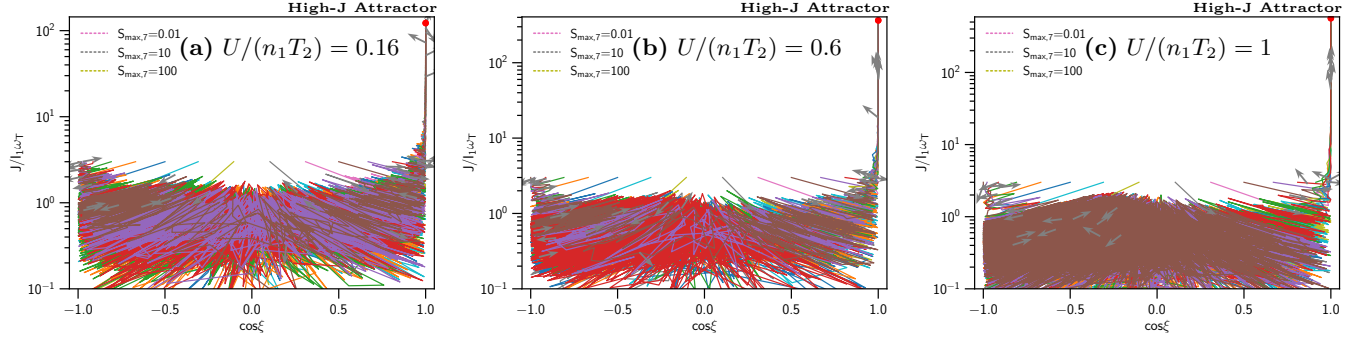


Figure 4. Phase trajectory maps of grain alignment for the different radiation fields of $U/(n_1 T_2) \leq 1$ (panels (a)-(c)), in the collision-dominated regime, assuming the RAT model of $q^{\max} = 2$ and SPM grains with $\delta_{\text{mag}} = 10^3$. Grains are rapidly spun up to the high-J attractor (red filled circles), but the majority of grains are driven to low-J rotation. Subsequently, gas and magnetic excitations strongly disturb the grain orientation at low-J rotation and scatter them into stable high-J attractors. Rotational disruption cannot occur due to low radiation strength.

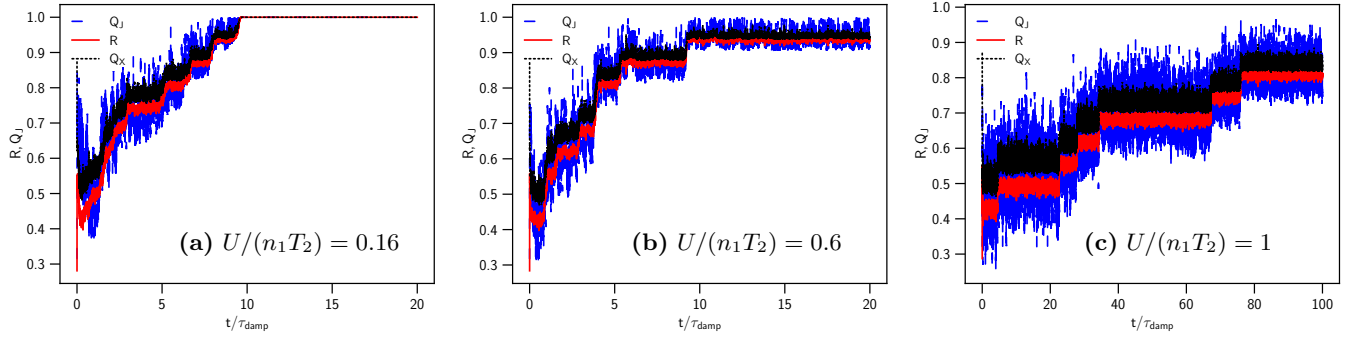


Figure 5. Same as Figure 4 but for the time-dependent alignment degrees Q_X, Q_J and R . The alignment degrees increase with time due to the transport of grains to high-J attractors by gas and magnetic excitations and achieves perfect alignment of $R \sim 1$ after $\sim 10\tau_{\text{damp}}$ for $U/(n_1 T_2) = 0.16, 0.6$ (panels (a),(b)) and near perfect alignment of $R \sim 0.8$ after $T_{\text{PA}} \sim 70\tau_{\text{damp}}$ (panel (c)).

Table 1. Model parameters, the damping and perfect alignment timescales for $q^{\max} = 2$ and $a_{\text{eff}} = 0.2 \mu\text{m}$.

$n_{\text{H}} (\text{cm}^{-3})$	U	$U/(n_1 T_2)$	δ_{mag}	$\tau_{\text{damp}} (\text{yr})$	$T_{\text{PA}} (\tau_{\text{damp}})$
10	0.1	0.16	10^3	$4.3 \times 10^5 n_1^{-1}$	10
—	0.5	0.6	—	$3.1 \times 10^5 n_1^{-1}$	20
—	1	1.0	—	$2.5 \times 10^5 n_1^{-1}$	70
10	0.1	0.16	1	$4.3 \times 10^5 n_1^{-1}$	50
—	0.5	0.6	—	$3.1 \times 10^5 n_1^{-1}$	70
—	1	1.0	—	$2.5 \times 10^5 n_1^{-1}$	80
10	2	1.9	—	2.9×10^5	NA
—	5	4.1	—	1.6×10^5	NA
—	10^1	7.3	—	9.9×10^4	NA
—	10^2	49.5	—	2.1×10^4	NA
—	10^3	337	—	4.6×10^3	NA
—	10^4	2296	—	9.9×10^2	NA
—	10^5	15640	—	2.1×10^2	NA

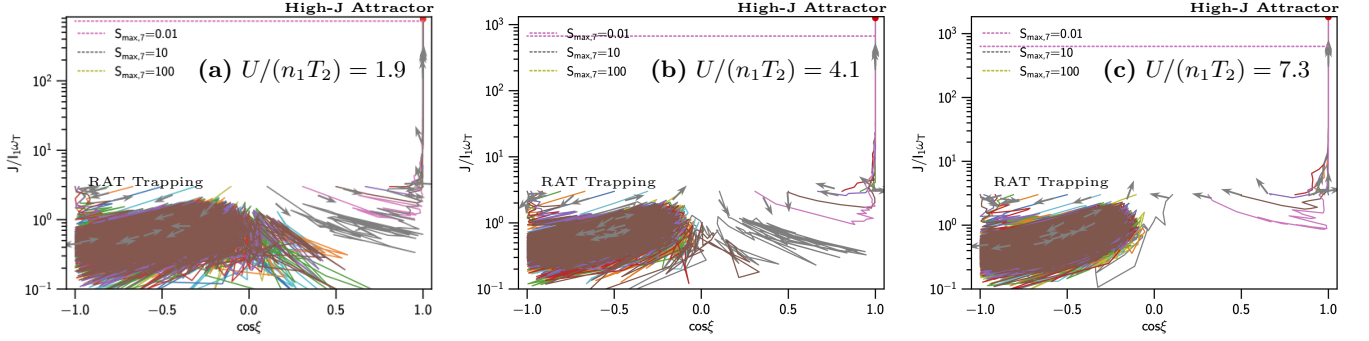


Figure 6. Same as Figure 4 but for the radiation-dominated regime with different $U/(n_1 T_2)$ (panels (a)-(c)). A fraction of grains are rapidly driven to the high-J attractor, and some grains are driven to the low-J rotation and trapped there by strong radiative torques. Collisional and magnetic excitations strongly disturb grain alignment but cannot scatter them into high-J rotation. Rotational disruption can occur for weak grains of $S_{\max,7} = 0.01$ (pink dotted line), even when grains are not yet reaching a high-J attractor.

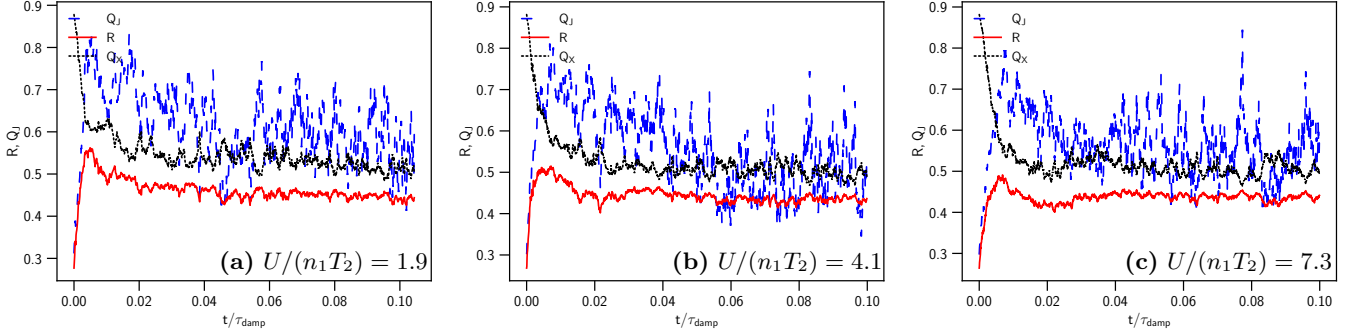


Figure 7. Same as Figure 6 but for the time-dependent alignment degrees. Within $0.01\tau_{\text{damp}}$, the external and net alignment degrees (Q_J, R) increase rapidly due to external alignment by MRATs, but the internal alignment degree Q_X decreases due to the damping of the grain angular momentum. Afterward, the alignment degrees decrease and slowly change after $t \sim 0.02\tau_{\text{damp}} \sim 0.02\tau_{\text{gas}}$ due to radiative torque trapping, although the external alignment is still fluctuating due to gas and magnetic excitation.

paramagnetic excitations that enhance the scattering of grains out of the low-J rotation to high-J attractors.

Figure 10 shows the alignment map for the RAT model of $q^{\max} = 1$ without high-J attractors and PM grains of $\delta_{\text{mag}} = 1$ in the CD regime. Collisional and magnetic excitations completely randomize grain alignment in the low-J rotation due to the lack of high-J attractors.

Figure 11 shows the alignment degrees for the case of $q^{\max} = 1$ and PM grains of $\delta_{\text{mag}} = 1$ (without a high-J attractor) in the CD regime. Collisional and magnetic excitations completely randomize grain alignment in the low-J rotation, leading to negligible alignment of grains with the external alignment degree of $Q_J = 0$ and the net alignment of $R = 0$. Note that the degree of internal alignment (Q_X) is still considerable due to the fast internal relaxation by Barnett relaxation, but Q_X is lower for higher $U/(n_1 T_2)$ due to stronger RAT damping. This confirms our previous results on requiring high-J attractors for considerable alignment.

4.4. Extreme radiation fields and reduced efficiency of magnetic relaxation on the RAT alignment

Here we run the simulations for extreme radiation with $U = 10^2 - 10^5$ and $q^{\max} = 2$, assuming SPM grains of $\delta_{\text{mag}} = 10^3$. These extreme radiation regimes with warm/hot dust are quite abundant in astrophysics, including circumstellar regions, AGN torus, planetary systems, and supernova ejecta.

Figure 12 shows the alignment maps for the extreme radiation regime. The fraction of grains with fast alignment at high-J attractor decreases with increasing $U/(n_1 T_2)$ due to reduced efficiency of magnetic relaxation on the RAT alignment, as predicted in Figure 3. We note that for this model in the CD regime, grains are perfectly aligned, as shown in Figure 4. The trajectory of grains during low-J rotation is disturbed less for increasing $U/(n_1 T_2)$ due to stronger RAT trapping and reduction of magnetic excitations. One interesting result from Figure 12 is that grains heading to high-J attractor can be disrupted. Therefore, all grains that can survive are trapped at low-J rotation.

Figure 13 shows the time-dependent alignment degrees for the different $U/(n_1 T_2)$. The alignment degrees are much lower than in the RD regime shown in Figure 7. Moreover, the grain alignment degrees decrease with increasing $U/(n_1 T_2)$ due to reduced efficiency of magnetic relaxation. For $U/(n_1 T_2) > 10^4$, the alignment degree does not depend on the value of δ_{mag} due to the suppression of magnetic relaxation and is purely determined by RATs. The fraction of grains aligned at high-J attractors depends only on q^{\max} . Collisional and magnetic excitations slightly scatter grain orientation out

of the low-J attractor. We note that for this model in the CD regime, grains are perfectly aligned as shown in Figure 5.

We note that in the extreme radiation field, the alignment does not change significantly compared to the CD and RD regimes because only a fraction of grains with initial angle $\cos \xi \sim 1$ can be rapidly aligned with \mathbf{B} . However, their angular momenta increase with time due to further spin-up by RATs over time. Therefore, the disruption can occur within $10^{-2} \tau_{\text{damp}}$, which results in the rapid change in the grain size distribution and composition.

4.5. The Fraction of Grains with Fast Alignment and Disruption at High-J Attractors

To determine the fraction of grains that can rapidly align at high-J attractors in less than one damping time, we run simulations for an integration time of $T_{\text{obs}} = \tau_{\text{damp}}/2$ for different RAT models, magnetic relaxation, and radiation strengths, assuming a population of $N_{\text{gr}} = 32$ grains with initially random orientations. We consider $q^{\max} = 0.5 - 4$, which is the most probable range of RATs from an ensemble of random shapes in Herranen et al. (2019).

Figure 14 shows the fraction of grains that have fast alignment at high-J attractors, $f_{\text{high-J}}^{\text{fast}}$, for the different RAT models described by q^{\max} and magnetic relaxation δ_{mag} for different radiation strengths $U = 1, 10, 10^2$ and 10^4 (panels (a)-(c)). The maximum degree for PM grains of $\delta_{\text{mag}} = 1$ is $f_{\text{high-J}}^{\text{fast}} \sim 0.22$, whereas the alignment degree for SPM grains is higher for larger δ_{mag} , and it can reach $f_{\text{high-J}}^{\text{fast}} \sim 0.45$ for $\delta_{\text{mag}} = 10^3$. However, the fraction of $f_{\text{high-J}}^{\text{fast}}$ decreases with increasing $U/(n_1 T_2)$. For $U/(n_1 T_2) = 15640$, $f_{\text{high-J}}^{\text{fast}}$ depends weakly on δ_{mag} due to the reduced efficiency of magnetic relaxation, and reach $f_{\text{high-J}}^{\text{fast}} \sim 0.22$.

5. DISCUSSION

We generalize the MRAT theory for general astrophysical conditions characterized by the relative local radiation strength to the gas density $U/(n_1 T_2)$ and use numerical simulations to quantify the efficiency of grain alignment by the MRAT mechanism. We confirmed the previous results for the collision-dominated regime ($U/(n_1 T_2) \leq 1$) discovered new effects for radiation-dominated (RD) regime and extreme radiation fields of with $U/(n_1 T_2) > 1$. Below, we discuss in detail our results and implications for a variety of astrophysical environments, from the standard ISM to cold and dense star-forming regions to hot circumstellar environments.

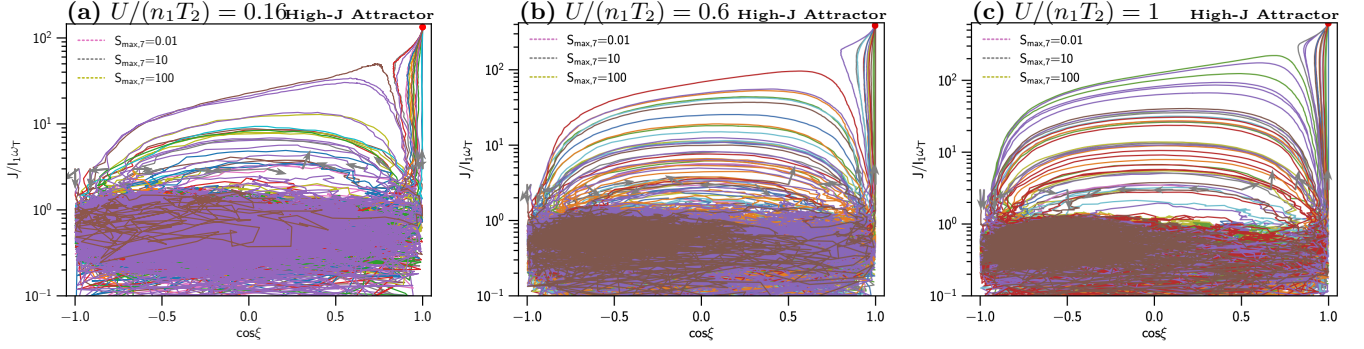


Figure 8. Same as Figure 4 but for PM grains with $\delta_{\text{mag}} = 1$. The phase trajectory during the low-J rotation is disturbed by collisional and magnetic excitations, but the trajectory for $J/I_1\omega_T > 3$ is deterministic due to reduced magnetic relaxation. All grains eventually reach the high-J attractor (red circle) by MRATs due to gas and magnetic excitations.

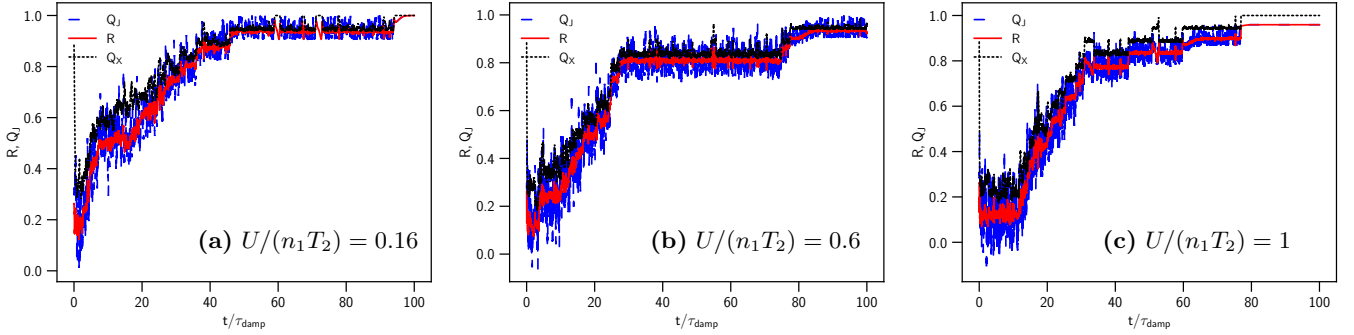


Figure 9. Same as Figure 5 but for PM grains with $\delta_{\text{mag}} = 1$. The alignment degree increases with time, but the time required to reach nearly perfect alignment is $T_{\text{PA}} \sim 80\tau_{\text{damp}}$ due to the reduced magnetic excitations.

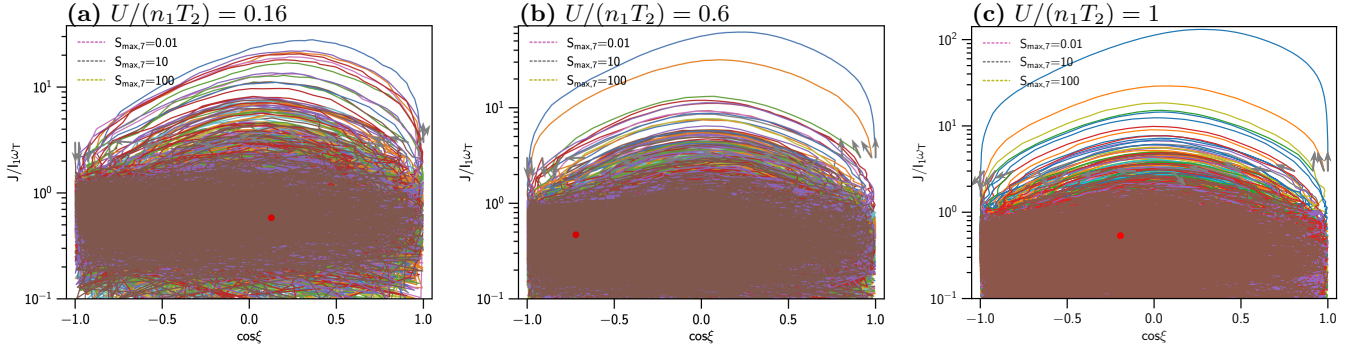


Figure 10. Same as Figure 4 but for PM grains with $\delta_{\text{mag}} = 1$ and the RAT model without high-J attractor of $q^{\text{max}} = 1$. The phase trajectory during the low-J rotation is significantly disturbed by collisional and magnetic excitations. All grains have cyclic trajectories during the suprathermal state of $J/I_1\omega_T > 3$ and randomly during $J/I_1\omega_T < 3$ due to gas and magnetic excitations.

5.1. Collision-Dominated (CD) Regime: Collisional and Magnetic Excitations Transporting Grains from low-J to High-J Attractors and Time-Dependent Alignment

In collision-dominated (CR) regimes, $U/(n_1 T_2) < 1$, the grain angular momentum experience strong fluctuations with respect to the ambient magnetic field during the slow rotation period due to gas random collisions and magnetic fluctuations (see Figure 4). Such fluctuations have two important consequences depending on the

MRAT properties. For grain alignment without a high-J attractor, fluctuations cause the randomization of \mathbf{J} and produce negligible alignment. However, when grain alignment has high-J attractors, fluctuations can slowly scatter grains from low-J to high-J attractors, resulting in the perfect alignment. These crucially essential effects were first discovered in Hoang & Lazarian (2008a) and further established in Hoang & Lazarian (2016a) for the diffuse ISM. In this paper, we conducted a comprehensive study of the MRAT alignment in general con-

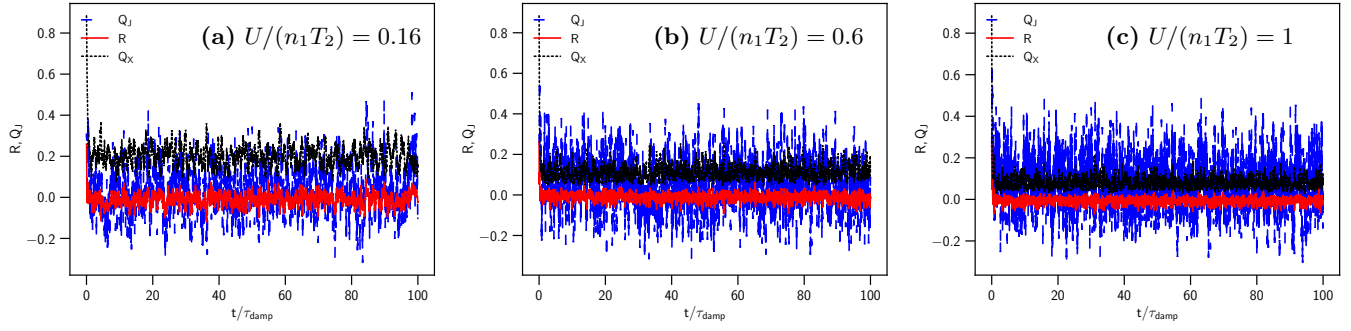


Figure 11. Same as Figure 5 but for PM grains with $\delta_{\text{mag}} = 1$ and $q^{\text{max}} = 1$. The net alignment degree R is zero due to collisional randomization for the RAT model without high-J attractors.

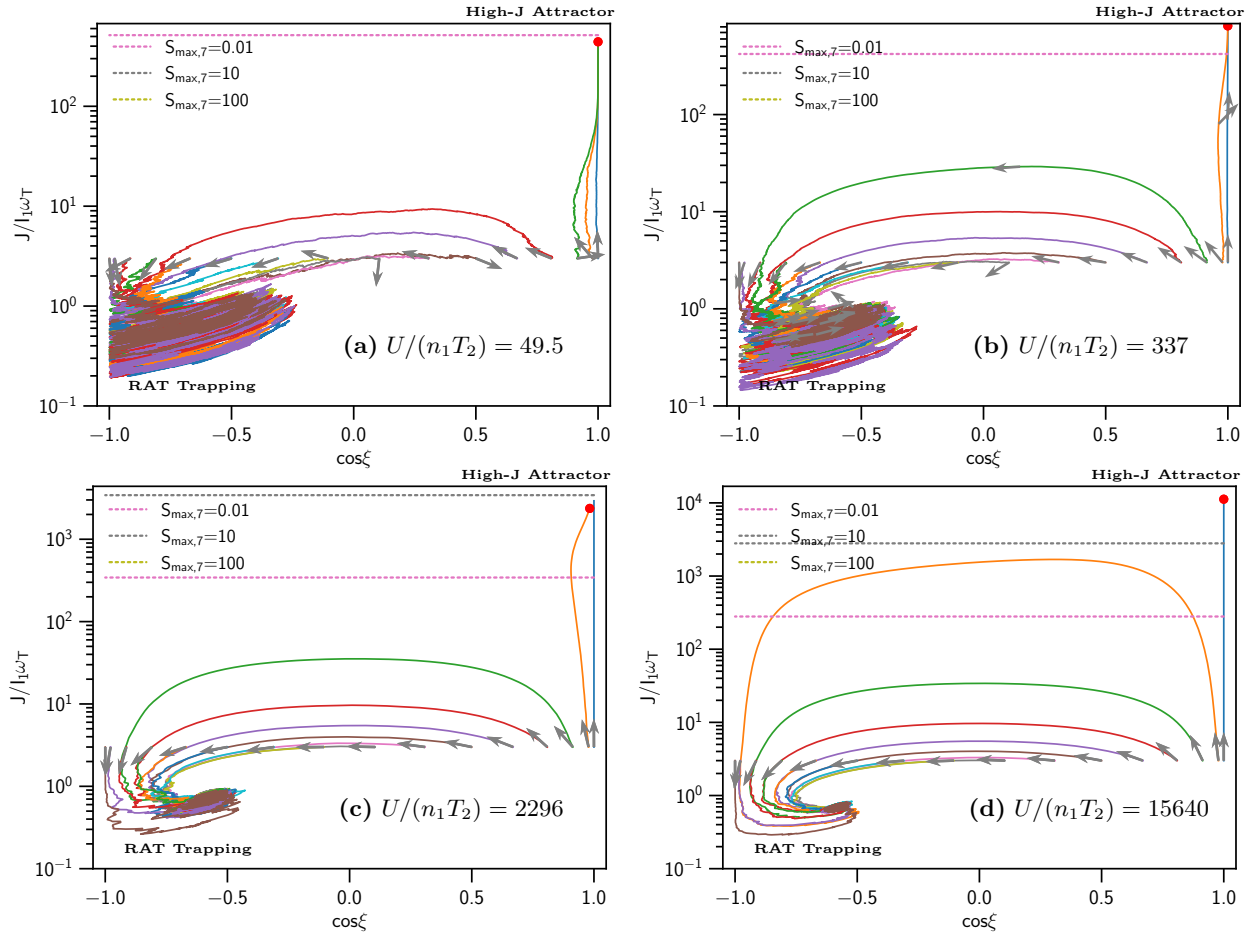


Figure 12. The phase trajectory map for the RAT model $q^{\text{max}} = 2$ and SPM grains with $\delta_{\text{mag}} = 10^3$ in extreme radiation fields with different $U/(n_1 T_2)$ (panels (a)-(d)). The fraction of grains with fast alignment at high-J attractor decreases with increasing $U/(n_1 T_2)$ due to reduced efficiency of magnetic relaxation. The trajectory of grains during low-J rotation is disturbed less for increasing $U/(n_1 T_2)$ due to stronger RAT trapping. Rotational disruption can occur even when grains are not yet reaching the high-J attractor.

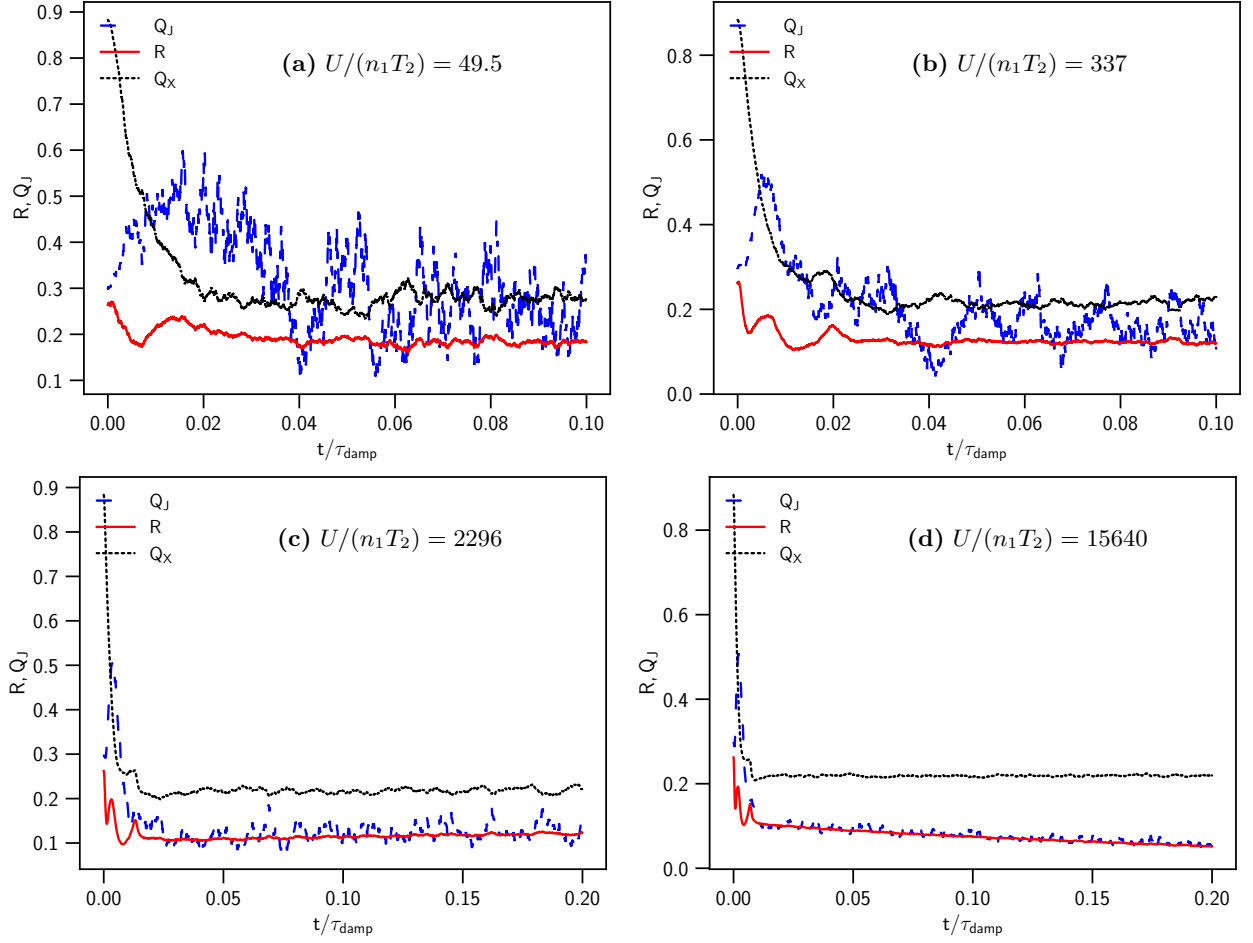


Figure 13. Same as Figure 12 but for time-dependent alignment degrees. Grain alignment degrees decrease with increasing $U/(n_1 T_2)$ due to reduced efficiency of magnetic relaxation. Fluctuations of external alignment Q_J (blue line) caused by gas and magnetic excitations at low- J rotation is much weaker for stronger radiation fields due to RAT trapping effect.

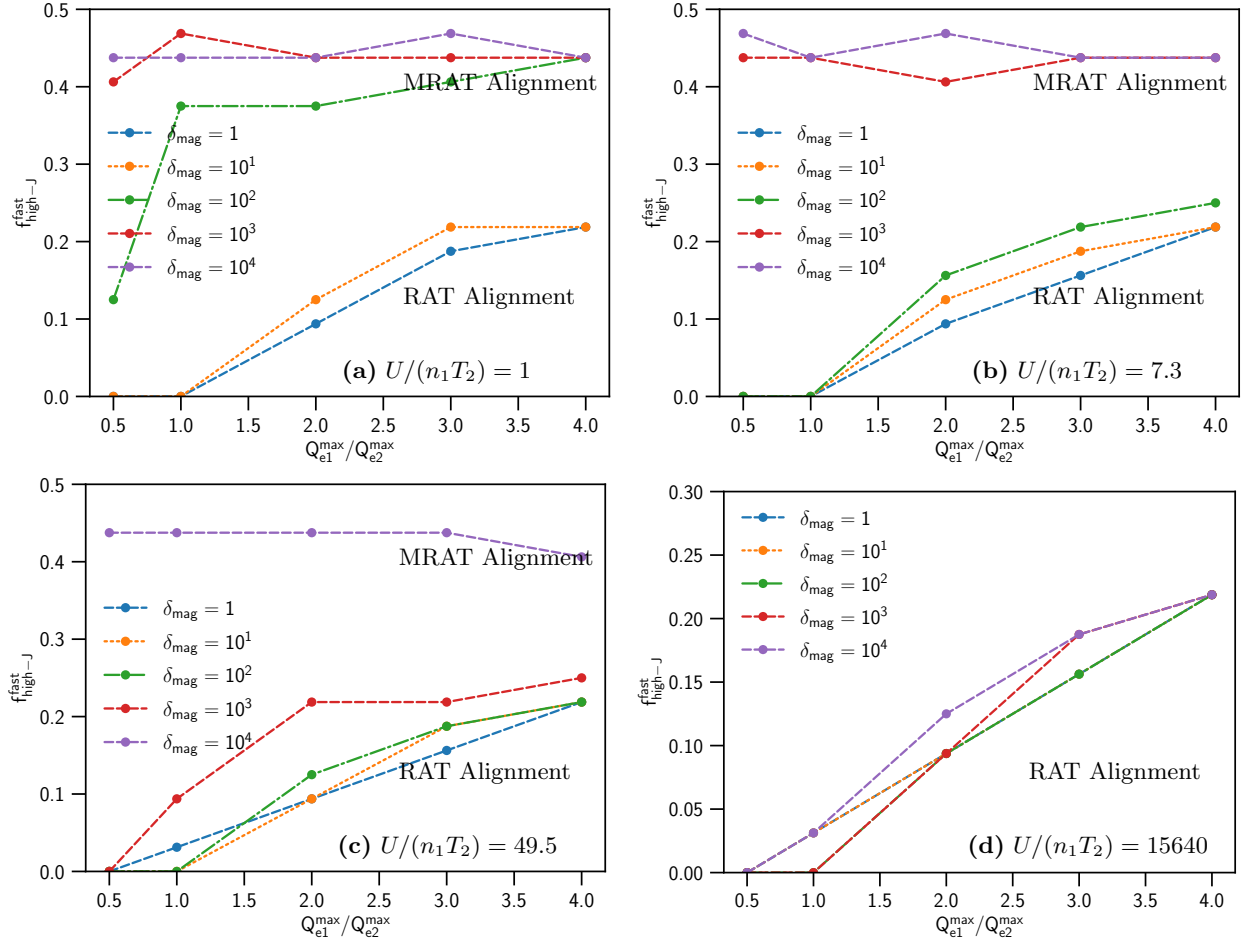


Figure 14. The fraction of grains with initial random orientation that undergo fast alignment with high-J, $f_{\text{high-J}}^{\text{fast}}$, for different RAT parameters and magnetic relaxation, assuming $\psi = 0^\circ$ for the different radiation fields $U/(n_1 T_2)$ (panels (a)-(d)). The value of $f_{\text{high-J}}^{\text{fast}}$ increases with δ_{mag} except for $U/(n_1 T_2) = 15640$ where magnetic relaxation becomes ineffective and alignment is dominated by RATs.

ditions and confirmed the crucial role of collisional and magnetic excitations leading to the perfect alignment of grains with high-J attractors.

We also found that the alignment degrees increase slowly with time and achieve the perfect alignment after $T_{\text{PA}} \sim 10\tau_{\text{gas}}$ for SPM grains, but it requires $50\tau_{\text{gas}}$ for PM grains due to the contribution of magnetic excitations (see Figures 18); Table 1). Therefore, iron inclusions not only enhance grain alignment by high-J attractors but also increase the rate of transport of grains from low-J to high-J attractors. This time-dependent alignment will induce time-dependent polarization. Therefore, we suggest observations of time-dependent polarization to constrain the magnetic property of dust.

In particular, our numerical simulations show that grain alignment is negligible if the high-J attractor points are absent in the collisional-dominated regime of $U/(n_1 T_2) < 1$. The detection of high polarization levels from the ISM (Planck Collaboration et al. 2015), molec-

ular clouds and filaments (Ngoc et al. 2023, Ngoc et al. 2024) to protostellar environments (Giang et al. 2024) strongly suggests that grains contain iron inclusions to induce universal high-J attractors, which cannot be produced by RATs only. Moreover, these observational results are strong evidence for the effect of collisional and magnetic excitations in transporting grains from low-J to high-J attractors and enabling highly efficient alignment of interstellar grains.

5.2. Radiation-Dominated (RD) Regime: Reduced Efficiency of Magnetic Relaxation and Radiative Torque Trapping

We identified three important effects for grain alignment in strong radiation fields in which radiation is dominant, $U/(n_1 T_2) > 1$. First, the effect of magnetic relaxation in enhancing the RAT alignment at high-J attractors is reduced at higher radiation fields due to faster driving grains to low-J attractors by RATs. Therefore,

to reproduce the same high-J attractors, the critical magnetic relaxation must be increased in stronger radiation fields (see Figure 3).

Second, we find the upper limit of the radiation field or dust temperature below which the magnetic relaxation is still effective in enhancing the RAT alignment. For the RAT model that does not produce high-J attractors (see Figure 3), magnetic relaxation is only effective for the radiation field of strength $U < U_{\max}^{\text{MRAT}} \sim 10^7 N_{\text{cl},5}^{3/2} \hat{B}^3$ (see Equation 43), or dust temperature $T_d < T_{\max}^{\text{MRAT}} \sim 220 N_{\text{cl},5}^{1/4} \hat{B}^{1/2}$ K (see Equation 44). Above these thresholds, magnetic relaxation does not affect grain alignment efficiency, and grains are entirely aligned by RATs. In this regime, the fraction of grain shapes with high-J attractors is $f_{\text{high-J}}^{\text{ens}} < 0.5$, and the fraction of grain orientations that can be directly lifted to high-J is $f_{\text{high-J}}^{\text{grain}} < 0.1$, which results in a net fraction of grains at high-J attractors of $f_{\text{high-J}} \sim 0.5 \times 0.1 = 0.05$ or 5% (see Figure 14).

Third, we found a new effect termed RAT trapping (RATT) in which strong radiative torques can trap grains at low-J rotation even in the presence of gas collisions and magnetic fluctuations when the radiation field is strong enough of $U/(n_1 T_2) > 1$. Gas random collisions and magnetic relaxation can scatter weakly grain orientation out of the low-J attractor (see Figures 6, 12). Therefore, for the RAT model without high-J attractors, RAT trapping can help increase the grain alignment efficiency by stabilizing grains at low-J attractors against random gas collisions. However, the net alignment degree is less than 20% due to low internal alignment due to slow grain rotation.

Finally, one important consequence of RAT trapping is that grains trapped at low-J rotation by intense radiation would have fast radiative precession and experience alignment along the radiation direction and experience k-RAT alignment (Lazarian & Hoang 2007; Lazarian & Hoang 2021)). This is a key signature of the RAT theory for the RD regions.

5.3. Radiative Torque Disruption: Fast and Slow Disruption and the Role of RAT Trapping

Fast-rotating grains can be disrupted due to their centrifugal stress. As shown in Figures 6 and 12, rotational disruption is related to grain alignment at high-J attractors, but some grains can be disrupted during their high-J rotation stage before being damped by RATs.

Our numerical calculations show that collisional and magnetic excitations can slowly transport grains from low-J to high-J attractors. When the grain angular velocity exceeds Ω_{cri} , they are disrupted into small fragments. This slow disruption takes a comparable time as

the time required for slow perfect alignment, which is between $10 - 100 \tau_{\text{gas}}$ in CD regimes. In the RD regime, the fast disruption can occur in less than τ_{damp} . However, the efficiency of fast disruption is much lower than that of slow disruption. To illustrate the fast disruption phenomenon, let us consider an ensemble of grains with different initial orientations and turn on a flash of intense radiation with a long duration. As shown in Figure 21, a fraction of grains driven rapidly to high-J attractors can experience fast disruption by RATD. The grain population with fast disruption includes grains initially already aligned with the magnetic field under the interstellar radiation field. The majority of grains are trapped at low-J rotation due to strong radiative torques and can survive strong radiation fields. The RAT trapping effect enables large grains to survive strong radiation fields, which is important for an accurate understanding of dust evolution and radiation pressure feedback.

The key difference between RATD and RAT trapping (RATT) is that RATD causes the depletion of large grains, but RATT helps large grains to survive in a strong radiation field by trapping them at low rotation. Both RATD and RATT reduce the polarization fraction, so the polarization degree alone is insufficient to distinguish the two mechanisms. Instead, we can combine the dust polarization with extinction curves and spectral index of thermal dust emission (SED) that provide constraints on maximum grain sizes. If large grains above a_{disr} are found in strong radiation fields, then, RATT is effective, while RATD is effective at lower efficiency. Moreover, we can also use the polarization angle and radiation direction. If large grains are dominantly trapped at low-J by RATT in strong radiation fields, we expect k-RAT instead of B-RAT.

5.4. Modeling Grain Alignment and Disruption Degree

The degree of grain alignment is dominated by the fraction of grains aligned at high-J attractors because grain alignment at low-J rotation is negligible due to collisional randomization. Let $f_{\text{high-J}}^{\text{ens}}$ be the fraction of grain shapes that have high-J attractors. In the AMO, the value of $f_{\text{high-J}}^{\text{ens}}$ depends on q^{max} . For an ensemble of random shapes with RATs calculated in Herranen et al. (2021), they found $f_{\text{high-J}}^{\text{ens}} \sim 0.2 - 0.6$. In the presence of iron inclusions, $f_{\text{high-J}}^{\text{ens}} = 1$ for $\delta_{\text{mag}} > \delta_{\text{cri}}$ (see Figure 3).

For a given grain shape, assume that grains initially have random orientations with respect to the magnetic field, then only a fraction of grains can be aligned at high-J attractors. Therefore, one can describe the fraction of grains at high-J attractors through both the fast

and slow alignment processes as

$$f_{\text{high-J}} = f_{\text{high-J}}^{\text{ens}} (f_{\text{high-J}}^{\text{fast}} + f_{\text{high-J}}^{\text{slow}}), \quad (59)$$

where $f_{\text{high-J}}^{\text{fast,slow}}$ is the fraction of grains with fast alignment and slow alignment. The alignment degree is then $R_{\text{align}} \approx f_{\text{high-J}}$.

Our numerical calculations of $f_{\text{high-J}}^{\text{fast}}$ for different models of RATs, magnetic relaxation, and local conditions are shown in Figure 14. Combined with our numerical calculations for the slow alignment, we obtain for SPM grains:

$$f_{\text{high-J}}^{\text{slow}} = 1 \text{ for } U/(n_1 T_2) \leq 1, \quad (60)$$

$$f_{\text{high-J}}^{\text{slow}} = 0 \text{ for } U/(n_1 T_2) > 1. \quad (61)$$

Therefore, in the CD regime, $R_{\text{align}} = f_{\text{high-J}}^{\text{ens}}$, and this regime is currently used in the ISM and SFRs. For the RD regime of extreme radiation field, $R_{\text{align}} = f_{\text{high-J}}^{\text{ens}} \times f_{\text{high-J}}^{\text{fast}}$.

In strong radiation fields, RATD is important for dust destruction and evolution. The RATD efficiency is given by

$$R_{\text{disr}} = f_{\text{high-J}}^{\text{ens}} \times f_{\text{high-J}}^{\text{fast}}, \quad (62)$$

which is a factor of 2 smaller than alignment efficiency R_{align} . Note that if initially grains are already aligned at high-J attractors and the radiation field is increased, then, those grains will be lifted further and will disrupt when $\Omega > \Omega_{\text{disr}}$. In this scenario, the RATD can reach the perfect disruption $R_{\text{disr}} = 1$.

5.5. Alignment and Disruption of Interstellar Dust in the ISM and Star-Forming Regions

5.5.1. The ISM, MCs to filaments and prestellar cores

In the ISM and star-forming regions, including filaments and prestellar cores, grains are subject to increasing density and decreasing radiation intensity. Along this star formation process, dust grains are present in the collision-dominated regions with $U/(n_1 T_2) < 1$ (Hoang et al. 2021b). Therefore, grains have enough time to be transported to high-J attractors, and slow alignment is efficient. Those thermally rotating grains will be aligned at higher-J by slow transport due to collisional and magnetic excitations, leading to perfect alignment over a timescale of

$$T_{\text{PA}} \sim 10 - 100 \tau_{\text{damp}} \sim 10^2 - 10^3 \left(\frac{10^4 \text{ cm}^{-3}}{n_{\text{H}}} \right) \text{ yr} \quad (63)$$

which is much shorter than the lifetime of the ISM and SFRs. Thus, one can achieve the perfect alignment of SPM grains by the MRAT mechanism.

Table 2. The typical phases of the ISM and parameters.

	CNM	WIM	PDR
$n_{\text{H}} (\text{cm}^{-3})$	30	0.1	10^4
$T_{\text{gas}} (\text{K})$	100	10^4	10^3
U	1	1	3×10^4
$U/(n_1 T_2)$	0.33	1	0.3

Those grains aligned with B-fields at high-J attractors and rotating suprathermally will be embedded into molecular clouds, which collapse to form protostars. Smaller grains will be damped by increasing gas collisions and radiation attenuation. Therefore, grains with iron inclusions in star-forming regions can be perfectly aligned with B-fields on high-J attractors due to slow transport from low-J to high-J attractors, i.e., $f_{\text{high-J}}^{\text{slow}} = 1$.

To illustrate the effect of local conditions, we run simulations for the cold neutral medium (CNM), warm-ionized medium (WIM), and photodissociation regions (PDR). Note that the WIM has much lower gas density but higher temperature than the CNM, whereas the PDR has much higher gas density and radiation fields. However, these three phases fall into the CD regime. Their physical parameters are shown in Table 2. Figures 15 and 16 show the phase trajectory maps and time-dependent alignment degrees obtained for these phases. As expected, grains in this CD regime can be perfectly aligned by slow transport of grains from low-J to high-J attractors, i.e., $f_{\text{high-J}}^{\text{slow}} = 1$. Interestingly, in both WIM and PDRs, which have very different gas properties and radiation fields from the CNM but a similar CD regime, collisional and magnetic excitations can efficiently transport grains from low-J to high-J attractors, leading to the perfect alignment within $10\tau_{\text{damp}}$.

5.5.2. Protostellar environments

Prestellar cores have a low radiation field and high density with $U/(n_1 T_2) < 1$, and they belong to the CD regime. Therefore, large grains of micron sizes with iron inclusions in prestellar cores and protostellar envelopes are already aligned by attenuated interstellar radiation by MRATs and achieve perfect alignment due to slow collisional and magnetic excitations (Hoang et al. 2022). As the central luminosity increases due to protostellar accretion and its blackbody emission, those grains at high-J attractors are further lifted to higher angular momentum.

Let us estimate the timescales for grain alignment in protostellar cores. The gas density and radiation strength at a distance r in the envelope from the proto-

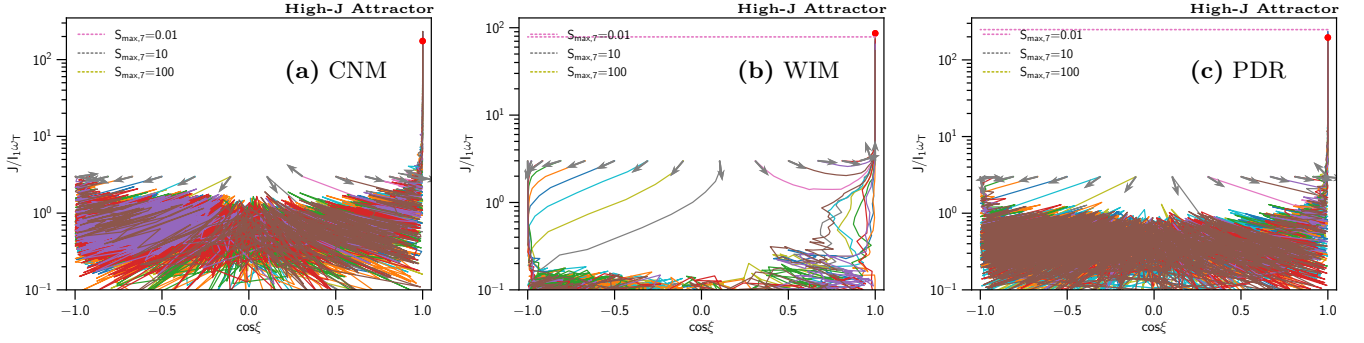


Figure 15. Phase trajectory maps for grain alignment in the CNM, WIM, and PDR, assuming the RAT model with $q^{\max} = 1$ and SPM grains of $\delta_{\text{mag}} = 10^3$. All grains align at the high-J attractor due to slow transport by gas collisions. Grains with low tensile strength can be disrupted in WIM and PDR.

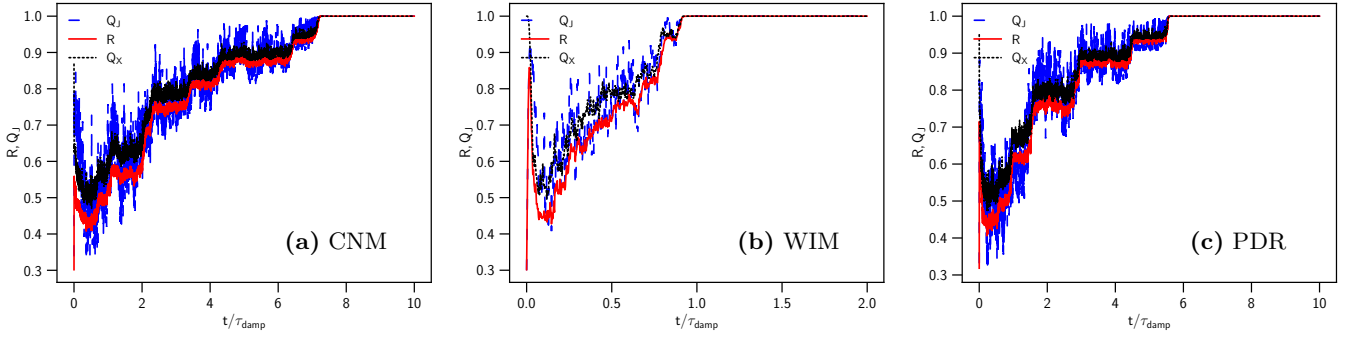


Figure 16. Time-dependent alignment degrees of grains in the CNM, WIM, and PDR. The alignment degrees increase with time due to slow transport by collisional excitations, and achieve perfect after $10\tau_{\text{damp}}$.

star are given by (Hoang et al. 2021b):

$$n_{\text{H}} \sim 10^6 \left(\frac{100 \text{ au}}{r} \right)^2 \text{ cm}^{-3}, \quad (64)$$

$$U \sim 5.2 \times 10^3 \left(\frac{100 \text{ au}}{r} \right)^2 \left(\frac{L_{\star}}{L_{\odot}} \right), \quad (65)$$

where the inner radius of the envelope is $r_{\text{in}} = 100 \text{ au}$, L_{\star} is the bolometric luminosity, and the attenuation by the intervening dust is disregarded. The equation yields $U/(n_1 T_2) \sim 10^{-3}$, which is well in the collision-dominated regime.

The rotational damping time is just the gas damping (Equation 1) due to the subdominance of IR emission, which is equal to

$$\tau_{\text{damp}} = \tau_{\text{gas}} \sim 10^{-1} \left(\frac{r}{100 \text{ au}} \right)^2 \text{ yr}. \quad (66)$$

Therefore, grain alignment takes about $T_{\text{PA}} \sim 10 - 100\tau_{\text{gas}} \sim 1 - 10 \text{ yr}$ to reach the perfect alignment by the MRAT (see e.g., 5). This timescale is much shorter than the dynamical time of protostellar cores, and one can assume the stable alignment.

One interesting effect arises when the protostellar luminosity suddenly increases due to episodic accretions. Indeed, episodic accretions onto protostars can increase

the luminosity by a factor of 100 (Audard et al. 2014), which entails $U/(n_1 T_2) \sim 0.1$, still in the CD regime. As a result, for episodic YSOs, increased radiation by the outburst will cause both fast and slow alignment of smaller grains over time, resulting in the time-dependent increase in the polarization degree. The polarization degree will reach the maximum level after a timescale of $T_{\text{PA}} \sim 10 - 100\tau_{\text{damp}} \sim 1 - 10 \text{ yr}$ due to the perfect alignment of grains by gas and magnetic excitations. This time-dependent polarization could be tested with the polarization survey for episodic YSOs, and the physics of slow alignment by MRAT could be tested.

5.5.3. HII bubbles around massive stars

HII regions (bubbles) are the ionized gas and dust shell produced by central massive stars (aka. Stromgren spheres). Gas is heated mainly by photoelectric effects of atomic hydrogen, while dust originating from the ISM (ISD) is heated by both stellar radiation and gas collisions. The typical gas temperature is $T_{\text{gas}} \sim 10^4 \text{ K}$, and dust temperature is $\sim 100 \text{ K}$ ($U \sim 4 \times 10^4$). The gas density is $n_{\text{H}} < 10^3 \text{ cm}^{-3}$, which corresponds to $U/(n_1 T_2) > 1$, so HII regions fall into the RD regime.

Since dust in HII bubbles mostly originates from the ISM, large grains have already been aligned at high-J

attractors by ISRF prior to massive star formation, and would be disrupted efficiently by massive stellar radiation. As a result, HII regions are expected to contain only small grains due to the depletion of large grains by RATD. We note that HII regions may contain newly formed dust from stellar winds of massive stars. For this stardust, grains can experience both RATD and RAT trapping, and the alignment and disruption degree is lower (see Figure 14).

For the local bubble, Medan & Andersson (2019) found the polarization efficiency $p/A_V \sim 0.1\%$ at $A_V = 1$, which is much lower than the maximum polarization efficiency observed in the ISM of $p/A_V \simeq 3\%/mag$. Such a lower polarization efficiency could be explained by both RATD and RAT trapping. Further observational polarization observations and data analysis are required to distinguish the RATD and RATT in HII regions.

5.6. Dust in active galactic nuclei (AGN) torus

Dust in the torus (1-10 pc) around supermassive black holes is subject to strong radiation fields from accretion disks. The gas density at a radial distance r in the torus is $n_H \sim n_{H0} r_{pc}^{-1} \text{ cm}^{-3}$ where $r_{pc} = r/1 \text{ pc}$. The radiation strength is approximated as $U(r) \sim 10^8 r_{pc}^{-2+\eta}$ where $\eta > 0$ accounts for the reddening by intervening dust (Giang & Hoang 2021). Therefore, one has $U/(n_1 T_2) \sim 10^4 (n_{H0}/10^5 \text{ cm}^{-3}) r_{pc}^{-\eta}$ where $T_{\text{gas}} \sim T_d \sim 20U^{1/6}$ is the gas temperature. Numerical calculations in Giang & Hoang (2021) shows $\eta \sim 3$ for $n_{H0} = 10^5 \text{ cm}^{-3}$, which yields $U/(n_1 T_2) > 1$ for $r < 10 \text{ pc}$. Therefore, grain alignment and disruption follow the RD regime.

Therefore, large grains of interstellar origin in the AGN torus may be rotating at high-J attractors and can be perfectly disrupted. However, the newly formed population experiences only the fast alignment and disruption due to RAT trapping.

5.7. Alignment and Disruption of Stardust in the Envelope of Evolved Stars

Circumstellar dust is the dust newly formed around stars from the condensation of gas expelled from stars (aka stardust). As soon as they are formed, stardust grains are thermally rotating and subject to strong radiation. This is radically different from ISD where grains are initially subject to average interstellar radiation and can be perfectly aligned at high-J attractors due to the slow transport process. Below, we describe briefly the typical parameters and discuss the alignment and disruption of stardust using our new general theory.

5.7.1. Stardust in the envelopes of evolved stars and planetary nebulae

The gas density and radiation strength in the envelopes of AGB stars can be given by (Tram et al. 2020)

$$n_H \simeq 10^6 \left(\frac{10^{15} \text{ cm}}{r} \right)^2 \left(\frac{\dot{M}}{10^{-5} M_\odot \text{ yr}^{-1}} \right) \text{ cm}^{-3}, \quad (67)$$

$$U \simeq 1.2 \times 10^8 \left(\frac{10^{15} \text{ cm}}{r} \right)^2 \left(\frac{L_\star}{10^4 L_\odot} \right), \quad (68)$$

where \dot{M} is the mass loss rate and L_\star is the bolometric luminosity of the evolved star.

For the gas temperature $T_{\text{gas}} \sim 200(r/10^{15} \text{ cm})^{-2}$ (Tram et al. 2020), Equations (67) and (68) yield the parameter $U/(n_1 T_2) \sim 500$, implying that the AGB envelopes fall into the radiation-dominated regime. Therefore, only a fraction of grains can be fast aligned at high-J attractors, and the rest of the grains are trapped at low-J rotations due to the RAT trapping (see Figure 6). However, collisional and magnetic excitations are inefficient in transporting them to high-J attractors due to RAT trapping, leading to the alignment $R = f_{\text{high-J}}^{\text{fast}} < 0.5$ (see Figure 14), which is a factor of 2 lower than in the collision-dominated regime of the ISM and SFRs where grain alignment can be perfect by the MRAT mechanism. The maximum degree of fast alignment is $R = f_{\text{high-J}}^{\text{ens}} \times f_{\text{high-J}}^{\text{fast}} > 0.5 \times 0.25 \sim 0.125$, assuming $f_{\text{high-J}}^{\text{ens}} = 0.5$ and $f_{\text{high-J}}^{\text{fast}} = 0.25$ for RAT alignment (see Figure 14).

5.7.2. Dust in the solar and exoplanetary systems

Dust in planetary systems is mainly produced from collisions of larger bodies and released from comets. Dust in planetary systems is warm and hot due to strong stellar radiation.

The radiation strength at distance r from a star of luminosity L_\star is given by

$$U \simeq 5.3 \times 10^7 \left(\frac{L_\star}{L_\odot} \right) \left(\frac{1 \text{ au}}{R} \right)^2, \quad (69)$$

where $L_\star = L_\odot$ for our solar system.

For the typical density of the local interplanetary medium is $n_H \sim 0.1 \text{ cm}^{-3}$ and $T_{\text{gas}} \sim 10^5 \text{ K}$, one obtains

$$\frac{U}{(n_1 T_2)} \sim 5.3 \times 10^6 \left(\frac{(L_\star/L_\odot)}{n_1} \right) \left(\frac{1 \text{ au}}{R} \right)^2. \quad (70)$$

Our results show that for this extreme radiation field of $U > U_{\text{max}}^{\text{MRAT}}$ (see Equation 43), grain alignment is entirely determined by RATs due to the suppression of magnetic relaxation. The maximum alignment degree is $R_{\text{max}} \sim 0.25$ as shown in Figure 14. Moreover, only grains that are fast aligned toward high-J attractors can

be disrupted, and slow transport is ineffective due to the strong radiation field. The disruption efficiency is $f_{\text{disr}} \sim f_{\text{high-J}}^{\text{ens}} \times f_{\text{high-J}}^{\text{fast}} \sim 0.1$ for the range of q^{max} as shown in Figure 14. This can better constrain the evolution of Zodiacal dust by the RATD effect (Hoang et al. 2021a; Ng et al. 2025) and help resolve the tension of beta meteoroids in the Zodiacal disk (Silsbee et al. 2025).

Therefore, the degree of alignment is $R_{\text{align}} \sim f_{\text{high-J}}^{\text{ens}} \times f_{\text{high-J}}^{\text{fast}} \sim 0.1$, resulting in a low degree of thermal dust polarization. We suggest high-sensitivity observations toward debris disks to test this prediction. Interestingly, ALMA has reported that a marginal detection of dust polarization is 0.51% Hull et al. (2022). Combining the total emission intensity (SED) and polarization of hot dust from exoplanetary systems would be crucial to test the RAT trapping.

Table 3 summarizes the main properties of RAT alignment, disruption, and trapping of interstellar dust and stardust in different environments.

6. SUMMARY

We generalized the MRAT theory for arbitrary radiation fields and gas density and used numerical simulations of the MRAT alignment to quantify the efficiency of grain alignment and disruption. Our main results are summarized as follows:

- We derive the critical magnetic relaxation strength for which grains of different shapes have high-J attractors due to the MRAT mechanism in general local gas density and radiation fields described by $U/(n_1 T_2)$. The critical relaxation must be increased in stronger environments $U/(n_1 T_2)$ to overcome the disalignment effect of RATs.
- We also derive the critical radiation field or dust temperature below which SPM relaxation is effective and grain alignment is described by the MRAT. For grains with embedded iron clusters, we found $T_{\text{max}}^{\text{MRAT}} \sim 220 N_{\text{cl},5}^{1/4} \hat{B}^{1/2}$ K. Above these thresholds, grain alignment is purely determined by RATs.
- We find that, for the collision-dominated (CD) regime of $U/(n_1 T_2) \leq 1$, collisional excitations can slowly transport large grains of $a_{\text{eff}} = 0.2 \mu\text{m}$ to high-J attractor and grains achieve perfect *slow alignment* within $\sim 10 - 100 \tau_{\text{gas}}$ to MRATs.
- For the radiation-dominated (RD) regime with $U/(n_1 T_2) > 1$, only a fraction of grains can be

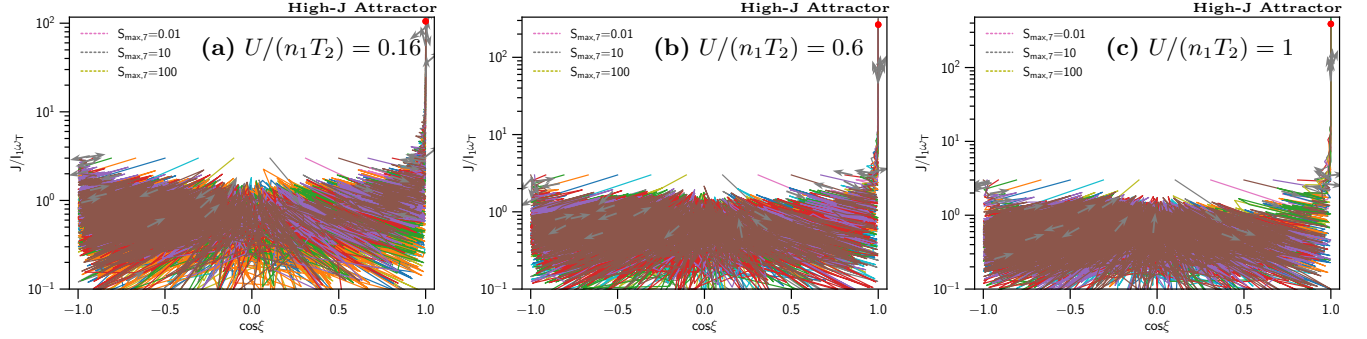
rapidly aligned at high-J attractors by MRATs, and the majority of grains are driven to low-J rotation and trapped there due to strong radiation, which is termed *radiative torque (RAT) trapping*. Grains only have the *fast alignment* by MRATs with the degree less than 50% in this RD regime.

- For extreme radiation fields of $U/(n_1 T_2) > 10^4$, we find that the efficiency of superparamagnetic relaxation in enhancing the RAT alignment is suppressed, and grains can have fast alignment and disruption purely determined by RATs with degrees below 23%.
- We found that magnetic relaxation and excitations become ineffective at extreme radiation fields of $U/(n_1 T_2) > \delta_{\text{mag}}$ due to the dominance of RATs, and grain alignment is determined by RATs only. Rotational disruption only occurs with a small fraction of grains with fast alignment to high-J attractor $f_{\text{high-J}}^{\text{fast}}$. We found that for strong radiation fields, grains can be rotationally disrupted during the alignment process of grains before being damped by RATs.
- We quantified the values of $f_{\text{high-J}}^{\text{fast}}$ for different RAT models, magnetic relaxation, and $U/(n_1 T_2)$. We find that the maximum $f_{\text{high-J}}^{\text{fast}}$ can reach 45% for SPM grains by the MRAT and 22% for the RAT mechanisms.
- We introduce a new parametric model for grain alignment efficiency based on the dimensionless parameter $U/(n_1 T_2)$. Our generalized MRAT theory can be applied to model grain alignment and disruption for different astrophysical environments, from the interstellar dust in the ISM and SFRs to stardust newly formed in the envelope of evolved stars and supernova ejecta.
- The newly discovered RAT trapping effect helps explain the existence of hot/warm large dust grains in stellar systems, AGN tori, and the survival of newly formed dust in the envelopes of evolved stars and supernova ejecta against RATD.

We thank Nguyen Chau Giang, Nguyen Bich Ngoc, and Nguyen Tat Thang for reading the first draft and for their useful comments. T.H. acknowledges the support from the main research project (No. 2025186902) from Korea Astronomy and Space Science Institute (KASI).

Table 3. Summary of RAT Alignment, Disruption and Trapping in different environments

Environments	$U/(n_1 T_2)$	Dust	RAT Alignment	RAT Disruption	RAT Trapping
ISM and SFRs	< 1	ISD	Fast and Slow	Fast and Slow	N
Evolved Star's Envelope	> 1	Stardust	Fast	Fast	Y
Planetary Systems	$\gg 1$	Stardust	Fast	Fast	Y
Supernova ejecta	$\gg 1$	Stardust	Fast	Fast	Y
AGN torus	> 1	ISD and Stardust	Fast and Slow	Fast and Slow	Y

**Figure 17.** Phase trajectory maps of grain alignment for the RAT model of $q^{\max} = 1$ and SPM grains with $\delta_{\text{mag}} = 10^3$ in the CD regime and different $U/(n_1 T_2)$ (panels (a)-(c)). Some grains rapidly spin up to the high-J attractor, and the rest of the grains are slowly transported to high-J attractors due to gas collisions and magnetic fluctuations.

APPENDIX

A. RESULTS FOR DIFFERENT MODELS OF THE RAT PROPERTIES, MAGNETIC PROPERTIES AND RADIATION FIELDS

Here we show the results for the different models of RATs with $q^{\max} = 1, 2, 3$ and SPM grains with $\delta_{\text{mag}} = 10^3$ for both CD and RD regimes. For this SPM grains, high-J attractors are always present regardless of the value of q^{\max} (see Figure 3). Therefore, we expect the results are similar to the case of $q^{\max} = 2$, but shows for completeness.

A.1. Results for different RAT Properties, q^{\max}

A.1.1. SPM grains in the collision-dominated regime

Figures 17 and 18 shows the phase map and time-dependent alignment degrees for the RAT model of $q^{\max} = 1$ and SPM grains of $\delta_{\text{mag}} = 10^3$ in the CD regime. Some grains are directly driven to high-J attractors, but the rest are first driven to low-J rotation, where gas collisions and magnetic relaxation transport grains to high-J attractors. Grain alignment degrees increase with time and achieve perfect alignment due to collisional and magnetic excitations of grains from low-J to high-J attractors.

Figures 19 and 20 show the phase map and time-dependent alignment degrees for $q^{\max} = 3$. The results are similar to the RAT model of $q^{\max} = 2$ shown in 4 and 5. This arises from the fact that for the SPM grains of $\delta_{\text{mag}} = 10^3$, grains have high-J attractors due to the MRAT (see Figure 3).

A.1.2. SPM grains in the radiation-dominated regimes

Figures 21 and 22 show the phase map and time-dependent alignment degrees for the RAT model of $q^{\max} = 1$ and SPM grains of $\delta_{\text{mag}} = 10^3$ in the RD regime. A fraction of grains is rapidly aligned at high-J attractor by the MRAT mechanism, but the majority of grains are driven to low-J and trapped there due to dominant radiative torques. Collisions and magnetic fluctuations can scatter grain orientation at low-J rotation, but are not strong enough to overcome RAT trapping. Grain alignment degrees increase rapidly first due to the MRAT alignment for a fraction

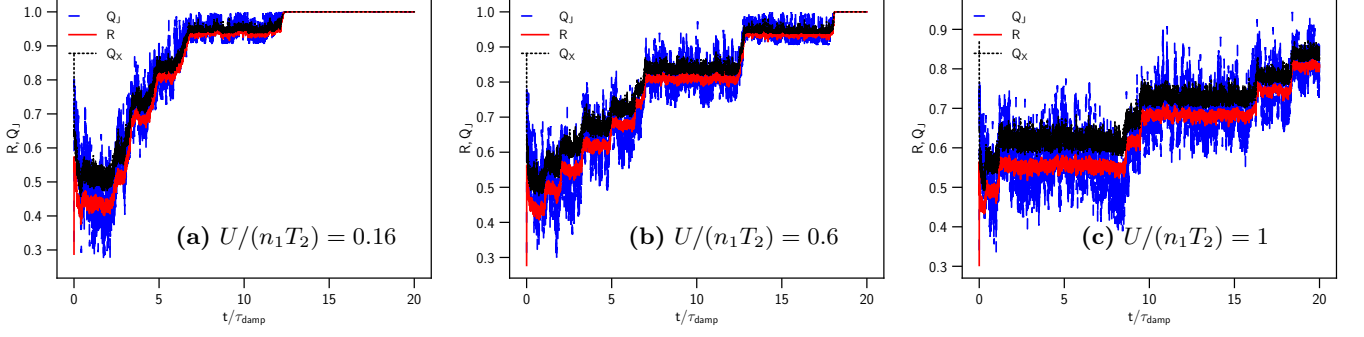


Figure 18. Same as Figure 17 but for temporal evolution of the alignment degrees. Alignment degree increases with time due to the random transport of grains to high-J attractors and achieves perfect alignment at $T_{PA} \sim 10 - 20\tau_{damp}$.

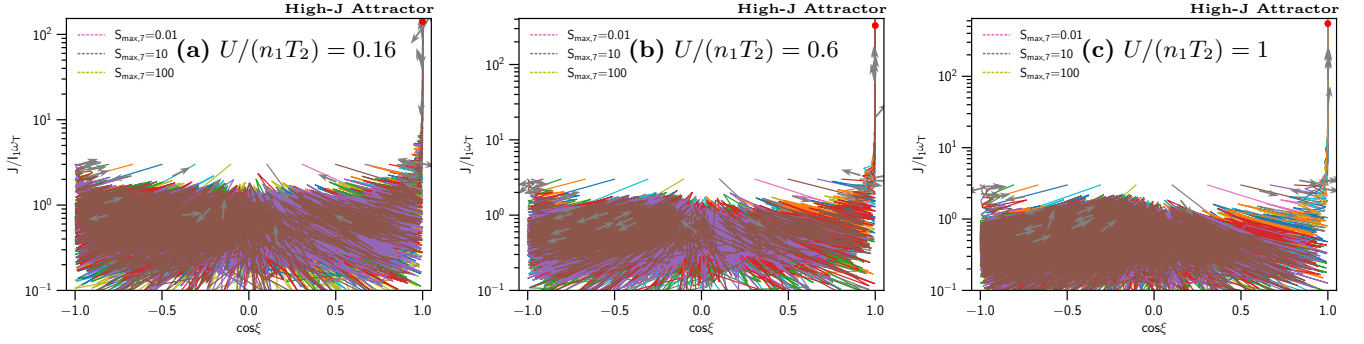


Figure 19. Phase trajectory maps of grain alignment for the RAT model of $q^{\max} = 3$ and SPM grains of $\delta_{\text{mag}} = 10^3$ in the CD regime of different $U/(n_1 T_2)$ (panels (a)-(c)). Some grains are rapidly spun up to the high-J attractor, but the rest of the grains are driven to the low-J rotation, followed by slow transport to high-J attractors by collisional and magnetic excitations.

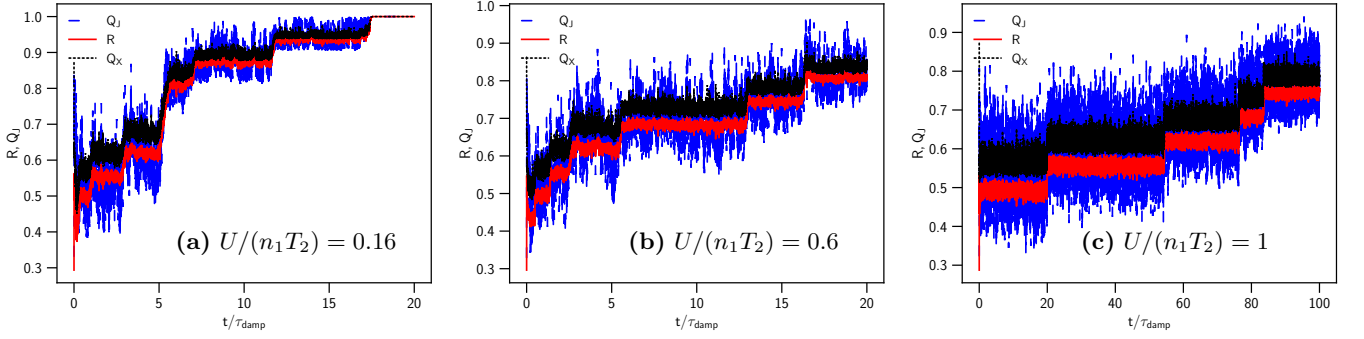


Figure 20. Same as Figure 19 but for temporal evolution of the alignment degrees. Alignment degree increases with time due to slow transport of grains to high-J attractors by collisional and magnetic excitations and achieve perfect at $T_{PA} \sim 20 - 100\tau_{damp}$.

of grains heading to high-J attractors, and then they get saturated at low alignment degrees due to RAT trapping of grains at low-J rotation.

Figures 23 and 24 show the phase-map and time-dependence alignment degrees for the RAT model of $q^{\max} = 3$ in the RD regime. The similar features are observed as in $q^{\max} = 1, 2$ because the high-J attractor is produced by SPM relaxation with $\delta_{\text{mag}} = 10^3$.

A.2. PM Grains in the CD and RD regimes

Figures 25 and 26 shows the alignment map and time-dependent alignment degrees for the RAT model of $q^{\max} = 3$ and PM grains of $\delta_{\text{mag}} = 1$ in the CD regime. A fraction of grains is rapidly aligned at high-J attractor, but the majority is first driven to low-J rotations, during which collisional and magnetic excitations slowly transport them to high-J attractor. The alignment degrees increase with time and reach perfect slow alignment after $50 - 100\tau_{damp}$.

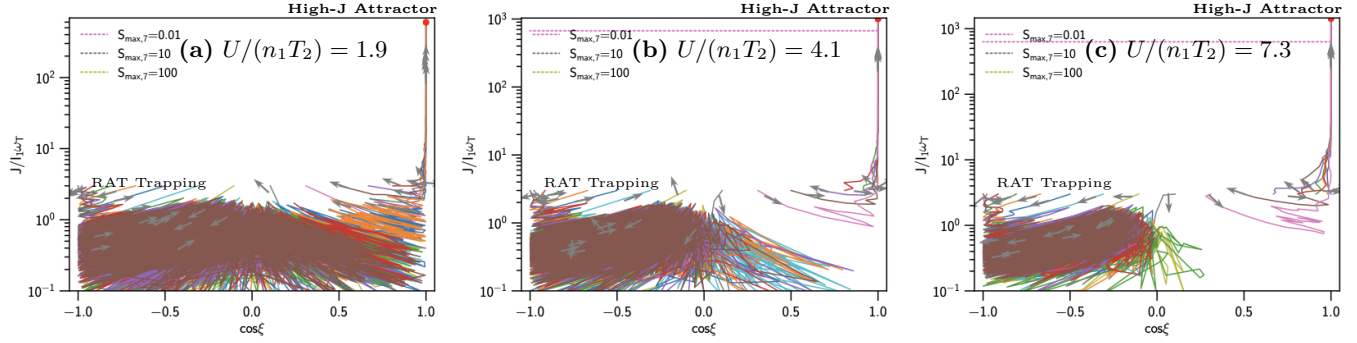


Figure 21. Phase trajectory maps of grain alignment for the RAT model of $q^{\max} = 1$ and SPM grains of $\delta_{\text{mag}} = 10^3$ in the RD regime with different $U/(n_1 T_2)$ (panels (a)-(c)). The value of γ is fixed. Some grains are driven rapidly to be aligned at the high-J attractor, and the rest of the grains are driven to low-J rotation and trapped by the RAT trapping.

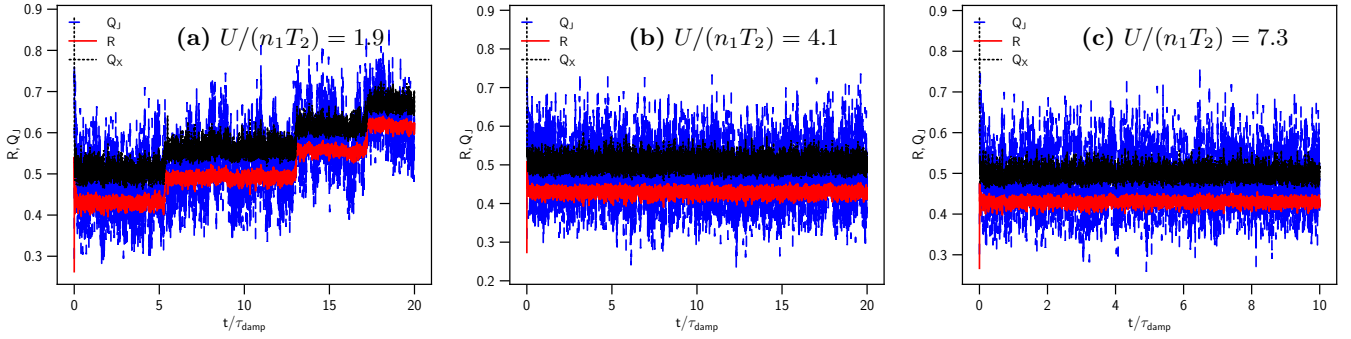


Figure 22. Same as Figure 21 but for temporal evolution of the alignment degrees. Alignment degree increases rapidly within $0.01\tau_{\text{damp}}$ and becomes saturated at $R \sim 0.4$ for intense radiation due to RAT trapping.

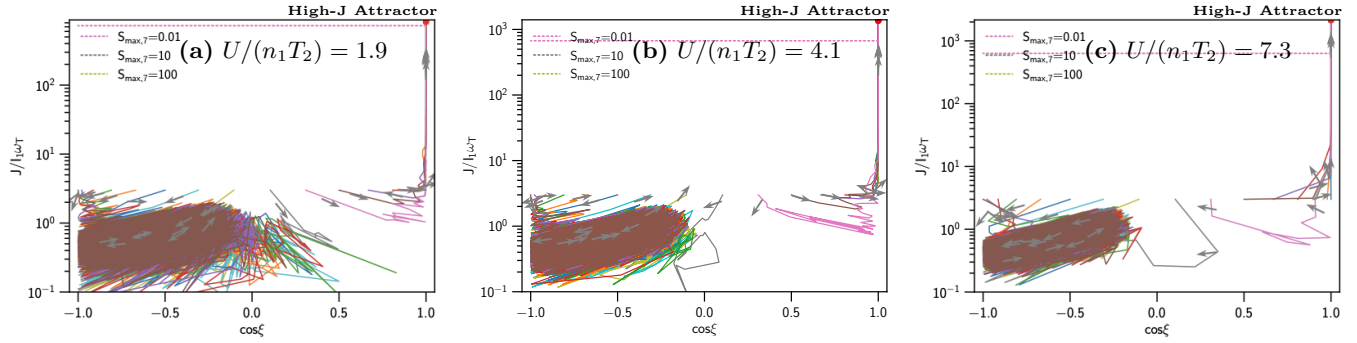


Figure 23. Phase trajectory maps of grain alignment for the RAT model of $q^{\max} = 3$ and SPM grains of $\delta_{\text{mag}} = 10^3$ in the RD regime of different $U/(n_1 T_2)$ (panels (a)-(c)). Some grains are driven rapidly to be aligned at the high-J attractor, and the rest of the grains are driven to low-J rotation and trapped by the RAT trapping.

Compared to Figure 20 for SPM grains, one can see that the timescale for reaching the perfect alignment is longer by a factor of 5 for the PM grains. This can be understood due to the effect of magnetic excitations that facilitate the scattering of grains out of the low-J rotation to high-J attractors.

Figure 27 shows the phase map for the RAT model of $q^{\max} = 3$ and PM grains of $\delta_{\text{mag}} = 1$ for the RD regime. Collisional and magnetic excitations are insufficient to significantly scatter grain orientations to transport them to high-J attractors compared to the CD regime. Figure 28 shows the time-dependent alignment degrees. Grain alignment is caused by grains with fast alignment at high-J attractors and is saturated due to RAT trapping of grains at low-J rotation.

Figures 29 and 30 show the phase alignment maps and time-dependent alignment degrees for the RAT model of $q^{\max} = 1$ and PM grains in the RD regime. Grain alignment is negligible due to the lack of high-J attractors.

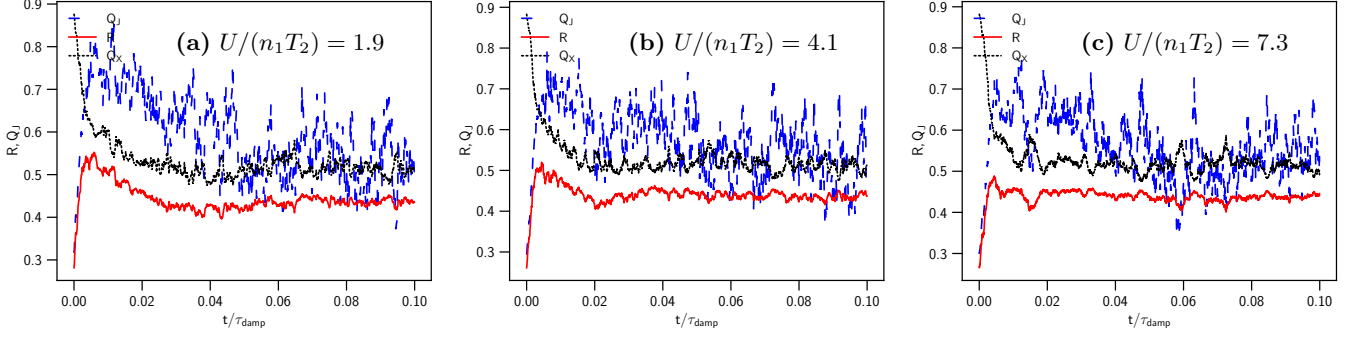


Figure 24. Same as Figure 23 but for temporal evolution of the alignment degrees for $\delta_{\text{mag}} = 10^3$. Alignment degrees increase rapidly within $0.01\tau_{\text{damp}}$ and become saturated at $R \sim 0.45$ for intense radiation due to RAT trapping.

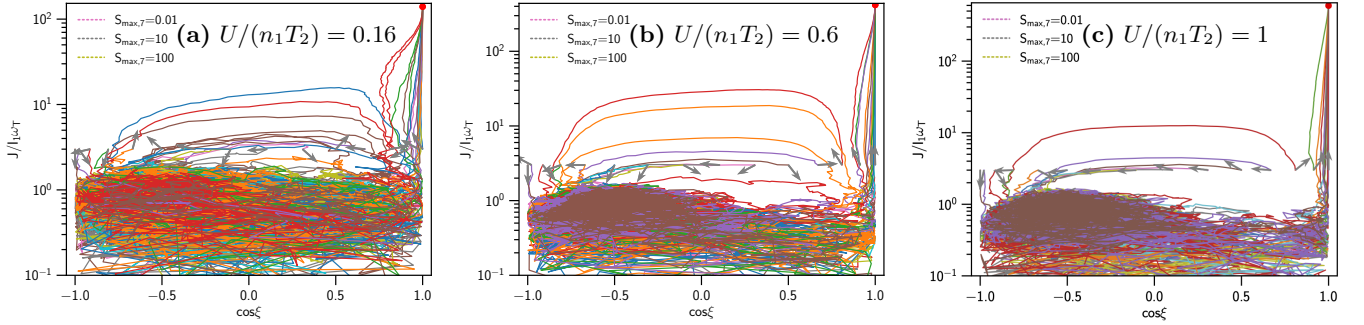


Figure 25. Phase-map for PM grains of $\delta_{\text{mag}} = 1$ and the RAT model of $q^{\text{max}} = 3$ in CD regime of different $U/(n_1 T_2)$ (panels (a)-(c)). Grains are eventually aligned at high-J attractors by RATs due to collisional and magnetic excitations.

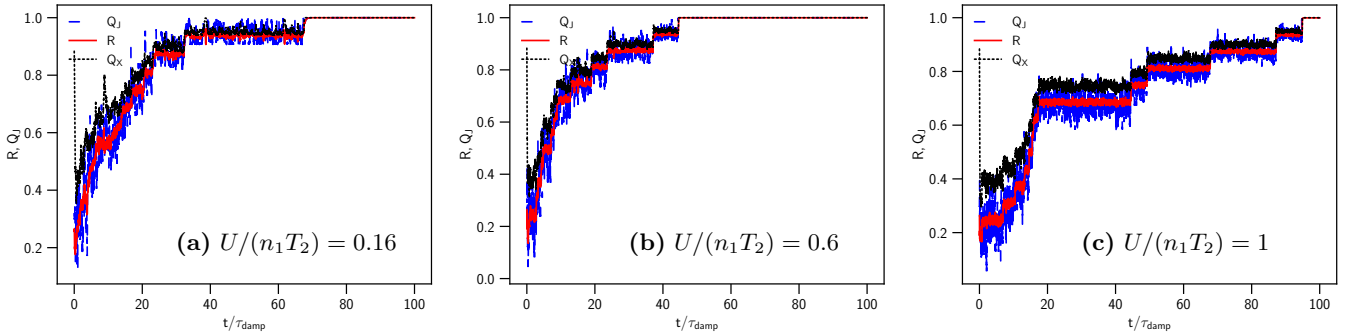


Figure 26. Same as Figure 25 but for the time-dependent alignment. Grain alignment degrees slowly increase with time and reach perfect alignment after $50 - 100\tau_{\text{damp}}$.

A.3. SPM Grains in Extreme Radiation Fields

In Figure 31, we show the results for SPM grains using the RAT model of $q^{\text{max}} = 3$ in extreme radiation fields. A fraction of grains is fast aligned at high-J attractors, whereas the rest is driven to low-J rotation and trapped there due to RAT trapping. The degrees of alignment shown in Figure 32) are less than 30% and become more stable for stronger radiation fields after a short initial period due to radiative trapping.

REFERENCES

- Andersson, B.-G., Lazarian, A., & Vaillancourt, J. E. 2015, ARA&A, 53, 501
- Audard, M., Ábrahám, P., Dunham, M. M., et al. 2014, arXiv.org, 1401, arXiv:1401.3368
- Barnett, S. J. 1915, Physical Review, 6, 239

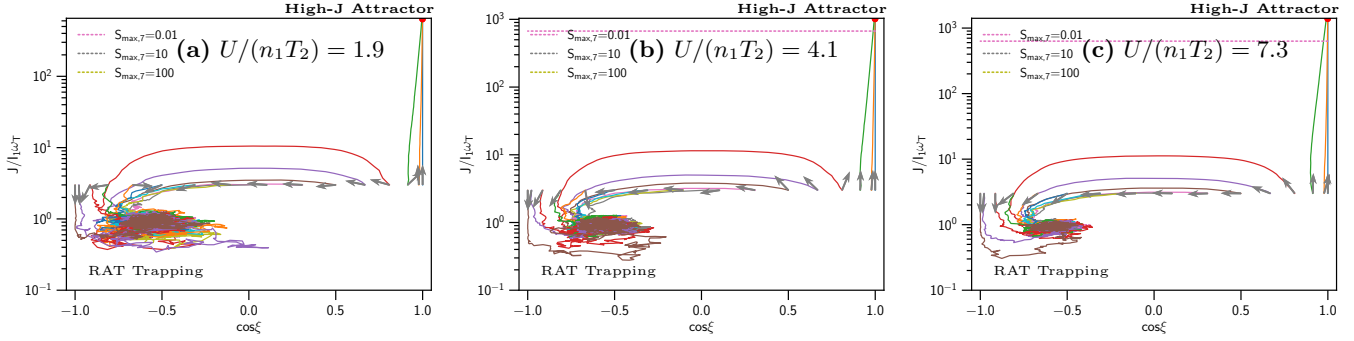


Figure 27. The phase alignment map for the RAT model of $q^{\max} = 3$ and PM grains of $\delta_{\text{mag}} = 1$ in the RD regime of different $U/(n_1 T_2)$ (panels (a)-(c)). Some grains are rapidly spun up to the high-J attractor, but the majority of grains are driven to low-J attractors and trapped at low-J rotation. Collisional and magnetic excitations are insufficient to significantly scatter grain orientations to transport them to high-J attractors compared to the CD regime, and grains are trapped by RATs.

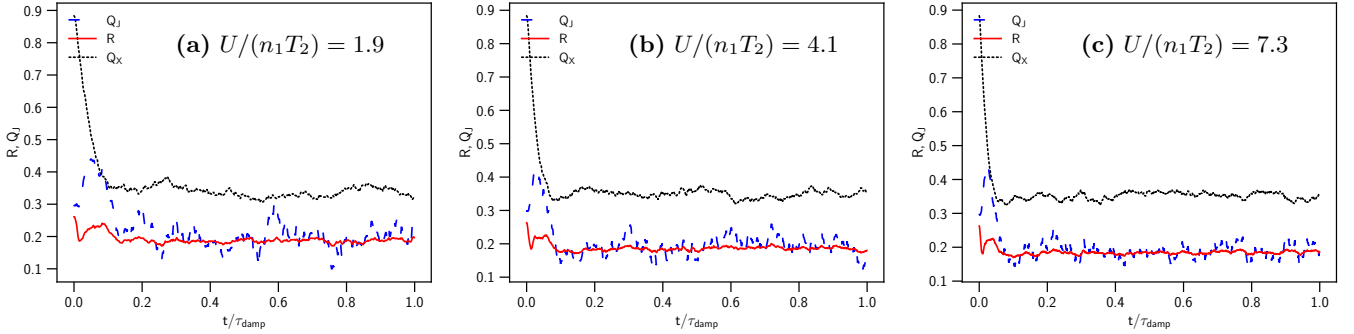


Figure 28. Same as Figure 27 but for time-dependent alignment. Alignment degree increases rapidly within $0.01\tau_{\text{damp}}$ and becomes saturated at $R \sim 0.2$ for intense radiation due to RAT trapping.

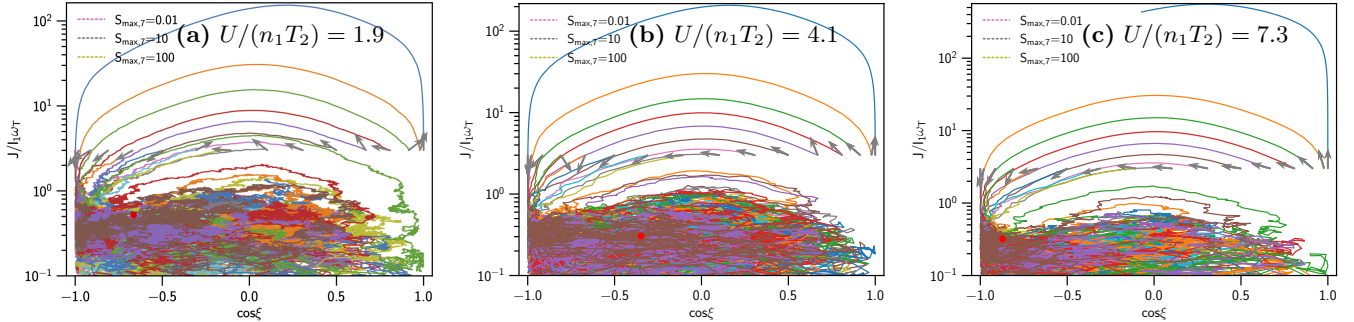


Figure 29. Same as Figure 27 but for $q^{\max} = 1$. Grains have no high-J attractors and undergo a random trajectory at low-J rotation.

Cugnon, P. 1983, A&A, 120, 156

Davis, L. J., & Greenstein, J. L. 1951, ApJ, 114, 206

Dolginov, A. Z., & Mitrofanov, I. G. 1976a,
(Astronomicheskii Zhurnal, 19, 758

—. 1976b, Ap&SS, 43, 291

Draine, B. T. 1996, in Astronomical Society of the Pacific
Conference Series, Vol. 97, Polarimetry of the Interstellar
Medium, ed. W. G. Roberge & D. C. B. Whittet, 16

Draine, B. T. 2011, Physics of the Interstellar and
Intergalactic Medium (Princeton, NJ: Princeton Univ.
Press)

Draine, B. T., & Flatau, P. J. 1994, Journal of the Optical
Society of America A: Optic s and Image Science, 11,
1491

Draine, B. T., & Lazarian, A. 1998, ApJ, 508, 157

Draine, B. T., & Weingartner, J. C. 1996, ApJ, 470, 551

—. 1997, ApJ, 480, 633

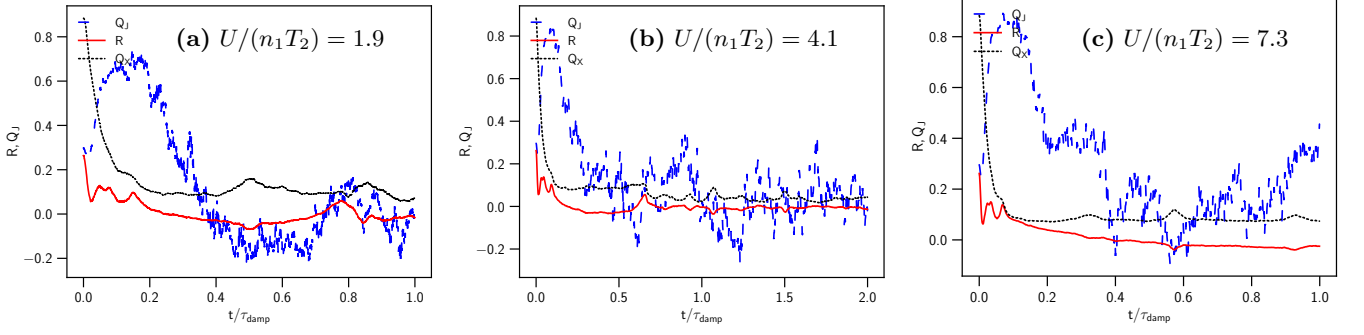


Figure 30. Same as Figure 29 but for time-dependent alignment. Grains have negligible alignment due to the lack of a high- J attractor.

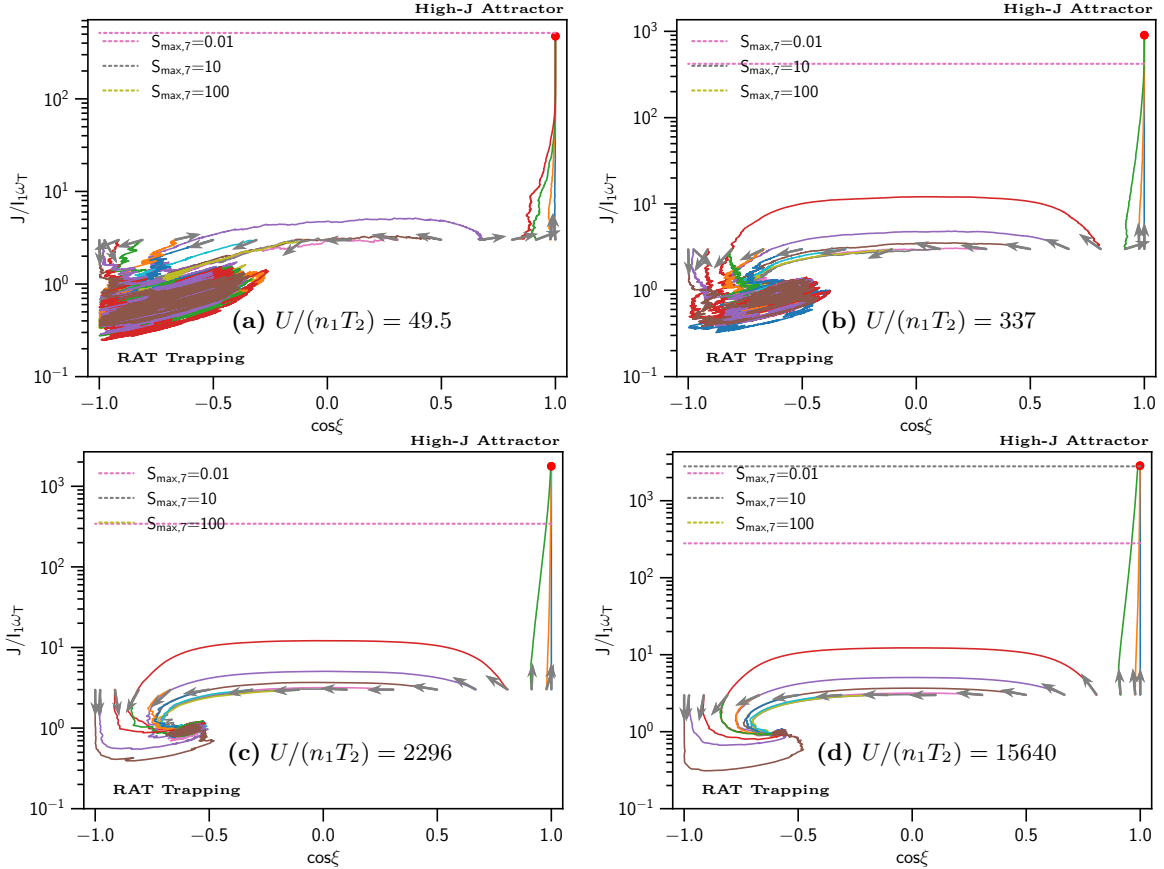


Figure 31. Phase-alignment map for the RAT model of $q^{\max} = 3$ and SPM grains of $\delta_{\text{mag}} = 10^3$ in extreme radiation fields (panels (a)-(d)). The fraction of grains that have fast alignment at high- J attractor decreases with increasing $U/(n_1 T_2)$ due to reduced efficiency of magnetic relaxation.

Giang, N. C., Gouellec, V. J. M. L., Hoang, T., Maury, A. J., & Hennebelle, P. 2024, arXiv, 2407.10079
 Giang, N. C., & Hoang, T. 2021, *The Astrophysical Journal*, 922, 47
 —. 2024, *Monthly Notices of the Royal Astronomical Society*, 530, 984
 Giang, N. C., Hoang, T., & Tram, L. N. 2020, *ApJ*, 888, 93
 Greenberg, J. M. 1968, in *Nebulae and Interstellar Matter*, ed. B. M. Middlehurst & L. H. Aller, 221

Hall, J. S. 1949, *Science*, 109, 166
 Herranen, J., Lazarian, A., & Hoang, T. 2019, *ApJ*, 878, 96
 —. 2021, *ApJ*, 913, 63
 Hiltner, W. A. 1949, *Nature*, 163, 283
 Hoang, T. 2019, *ApJ*, 876, 13
 —. 2022, *ApJ*, 928, 102
 Hoang, T., & Lazarian, A. 2008a, *MNRAS*, 388, 117
 —. 2008b, *MNRAS*, 388, 117
 —. 2009a, *ApJ*, 697, 1316

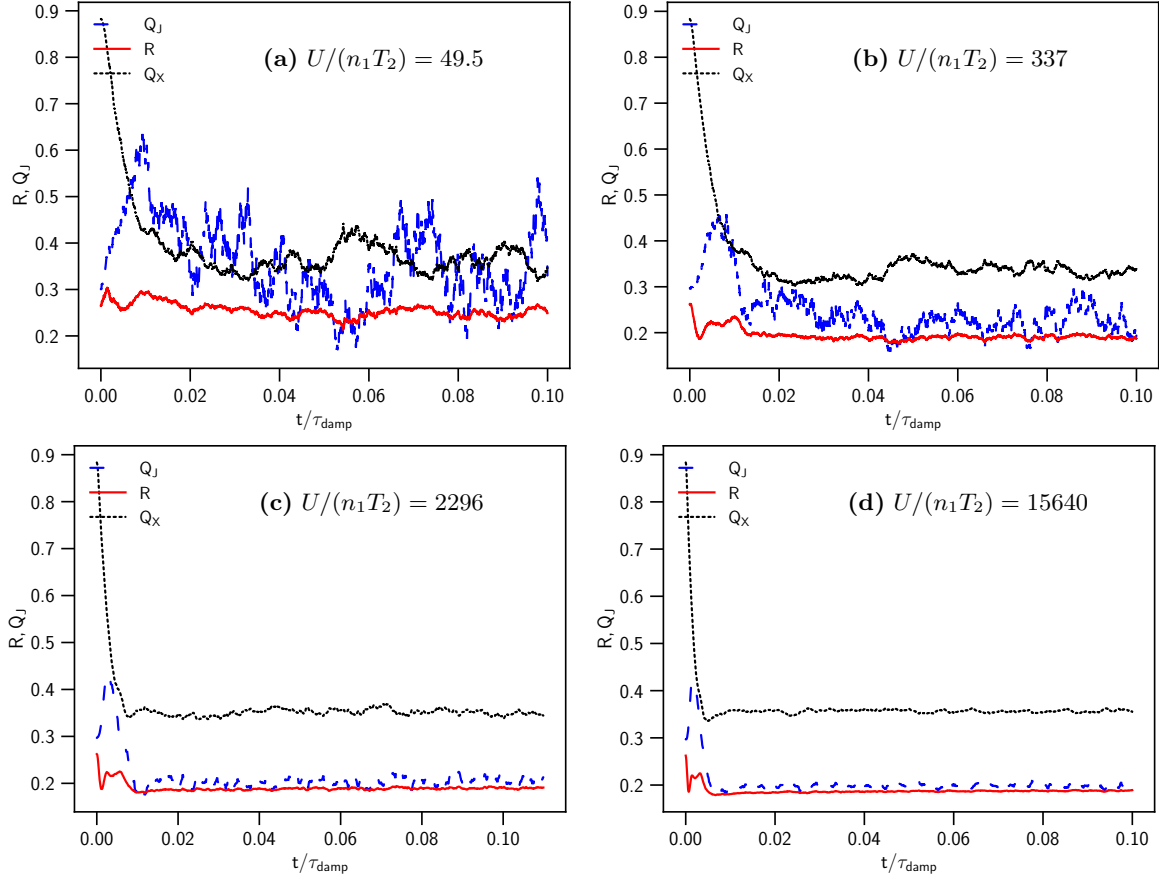


Figure 32. Same as Figure 32 but for time-dependent grain alignment. Grain alignment degree decreases with increasing $U/(n_1 T_2)$ due to reduced efficiency of magnetic relaxation.

—. 2009b, ApJ, 695, 1457

—. 2016a, ApJ, 831, 159

—. 2016b, ApJ, 821, 91

Hoang, T., Lazarian, A., & Draine, B. T. 2011, ApJ, 741, 87

Hoang, T., Lazarian, A., Lee, H., et al. 2021a, The Astrophysical Journal, 919, 91

Hoang, T., Lazarian, A., & Martin, P. G. 2014, ApJ, 790, 6

Hoang, T., Tram, L. N., Lee, H., & Ahn, S.-H. 2019, NatAs, 3, 766

Hoang, T., Tram, L. N., Lee, H., Diep, P. N., & Ngoc, N. B. 2021b, ApJ, 908, 218

Hoang, T., Tram, L. N., Minh Phan, V. H., et al. 2022, AJ, 164, 248

Hoang, T., & Truong, B. 2024, The Astrophysical Journal, 965, 183

Hoang, T., Vinh, N. A., & Quynh Lan, N. 2016, ApJ, 824, 18

Hull, C. L. H., Yang, H., Cortés, P. C., et al. 2022, The Astrophysical Journal, 930, 49

Jager, J. A., Reissl, S., & Klessen, R. S. 2024, Astronomy & Astrophysics, 692, A244

Jenkins, E. B. 2009, ApJ, 700, 1299

Jones, R. V., & Spitzer, L. 1967, ApJ, 147, 943

Lazarian, A. 1997, MNRAS, 288, 609

Lazarian, A., Andersson, B.-G., & Hoang, T. 2015, in Polarimetry of stars and planetary systems, ed. L. Kolokolova, J. Hough, & A.-C. Levasseur-Regourd ((New York: Cambridge Univ. Press)), 81

Lazarian, A., & Efrimsky, M. 1999, MNRAS, 303, 673

Lazarian, A., & Hoang, T. 2007, MNRAS, 378, 910

—. 2008, ApJ, 676, L25

Lazarian, A., & Hoang, T. 2021, ApJ, 908, 12

Mathis, J. S., Mezger, P. G., & Panagia, N. 1983, A&A, 128, 212

Medan, I., & Andersson, B.-G. 2019, The Astrophysical Journal, 873, 87

Ng, C.-H., Gu, P.-G., & Hoang, T. 2025, Monthly Notices of the Royal Astronomical Society, 538, 1944

Ngoc, N. B., Hoang, T., Diep, P. N., & Tram, L. N. 2024, The Astrophysical Journal, 974, 118

Ngoc, N. B., Diep, P. N., Hoang, T., et al. 2023, The Astrophysical Journal, 953, 66

- Pattle, K., Fissel, L., Tahani, M., Liu, T., & Ntormousi, E. 2023, in *Astronomical Society of the Pacific Conference Series*, Vol. 534, *Protostars and Planets VII*, ed. S. Inutsuka, Y. Aikawa, T. Muto, K. Tomida, & M. Tamura, 193
- Planck Collaboration, Ade, P. A. R., Aghanim, N., Alina, D., & et al. 2015, *A&A*, 576, A104
- Reissl, S., Wolf, S., & Brauer, R. 2016, *A&A*, 593, A87
- Roberge, W. G., Degraff, T. A., & Flaherty, J. E. 1993, *ApJ*, 418, 287
- Roberge, W. G., & Lazarian, A. 1999, *MNRAS*, 305, 615
- Silsbee, K., Hensley, B. S., Szalay, J. R., Pokorný, P., & Kim, J.-G. 2025, *The Astrophysical Journal Letters*, 982, L57
- Tram, L. N., & Hoang, T. 2022, *Frontiers in Astronomy and Space Sciences*, 9, 923927
- Tram, L. N., Hoang, T., Soam, A., Lesaffre, P., & Reach, W. T. 2020, *ApJ*, 893, 138
- Tram, L. N., Lee, H., Hoang, T., et al. 2021a, *ApJ*, 908, 159
- Tram, L. N., Hoang, T., Lopez-Rodriguez, E., et al. 2021b, *ApJ*, 923, 130
- Truong, B., & Hoang, T. 2024, *arXiv*, 2407.14896
- Truong, B., Tram, L. N., Hoang, T., et al. 2022, *The Astrophysical Journal*, 936, 101
- Tsukamoto, Y., Maury, A., Commercon, B., et al. 2023, in *Astronomical Society of the Pacific Conference Series*, Vol. 534, *Protostars and Planets VII*, ed. S. Inutsuka, Y. Aikawa, T. Muto, K. Tomida, & M. Tamura, 317
- Weingartner, J. C., & Draine, B. T. 2003, *ApJ*, 589, 289
- Yang, H. 2021, *ApJ*, 911, 125